

submitted 7AUG97, revised 23JAN98

# The Evolution of X-ray Clusters in a Low-Density Universe

Vincent R. Eke <sup>1</sup>

Department of Physics, Astrophysics, University of Oxford, Keble Road, Oxford OX1 3RH, England.

Julio F. Navarro <sup>2</sup>

Steward Observatory, University of Arizona, Tucson, AZ, 85721, USA.

Carlos S. Frenk <sup>3</sup>

Physics Department, University of Durham, Durham DH1 3LE, England.

## ABSTRACT

We present results of N-body/gasdynamical simulations designed to investigate the evolution of X-ray clusters in a flat, low-density,  $\Lambda$ -dominated cold dark matter (CDM) cosmogony. The simulations include self-gravity, pressure gradients and hydrodynamical shocks, but neglect radiative cooling. The density profile of the dark matter component can be fitted accurately by the simple formula originally proposed by Navarro, Frenk & White to describe the structure of clusters in a CDM universe with  $\Omega = 1$ . In projection, the shape of the dark matter radial density profile and the corresponding line-of-sight velocity dispersion profile are in very good agreement with the observed profiles for galaxies in the CNOC sample of clusters. This suggests that galaxies are not strongly segregated relative to the dark matter in X-ray luminous clusters. The gas in our simulated clusters is less centrally concentrated than the dark matter, and its radial density profile is well described by the familiar  $\beta$ -model. As a result, the average baryon fraction within the virial radius ( $r_{\text{vir}}$ ) is only 85-90% of the universal value and is lower nearer the center. The total mass and velocity dispersion of our clusters can be accurately inferred (with  $\sim 15\%$  uncertainty) from their X-ray emission-weighted temperature. We generalize Kaiser's scalefree scaling relations to arbitrary power spectra and low-density universes and show that simulated clusters generally follow these relations. The agreement between the simulations and the analytical results provides a convincing demonstration of the soundness of our gasdynamical numerical techniques. Although our simulated clusters resemble observed clusters in several respects, the slope of the luminosity-temperature relation implied by the scaling relations, and obeyed by the simulations, is in disagreement with observations. This suggests that non-gravitational effects such as preheating or cooling must have played an important role in determining the properties of the observed X-ray emission from galaxy clusters.

*Subject headings:* galaxies:clusters:general – cosmology:theory – dark matter – X-rays:general.

---

<sup>1</sup>E-mail: v.eke1@physics.oxford.ac.uk

<sup>2</sup>Bart J. Bok Fellow. E-mail: jnavarro@as.arizona.edu

<sup>3</sup>E-mail: C.S.Frenk@durham.ac.uk

## 1. Introduction

Galaxy clusters, the largest virialized systems in the universe, are useful cosmological probes. For example, the abundance of massive clusters (characterized either by mass or X-ray temperature) depends sensitively on  $\Omega_0$ , the cosmological density parameter, and on  $\sigma_8$ , the rms amplitude of density fluctuations on the fiducial scale  $8 h^{-1} \text{Mpc}$  (White, Efstathiou & Frenk 1993, Eke, Cole & Frenk 1996, Viana & Liddle 1996). Thus, the present-day abundance of clusters and its redshift evolution may be used to place constraints these two fundamental cosmological parameters. Similarly, the observed baryon fraction in clusters places strong constraints on the value of  $\Omega_0$  (White et al. 1993). Recent applications of these ideas tend to favor low values of  $\Omega_0 \simeq 0.3$  (White & Fabian 1995, Evrard 1997, Henry 1997) and, for flat models with this  $\Omega_0$ , values of  $\sigma_8 \simeq 1$  which are broadly consistent with the amplitude of the microwave background anisotropies measured by COBE (Smoot et al. 1992).

To exploit fully the cosmological information encoded in the cluster population, it is necessary to understand their evolutionary history in some detail. This requires modeling the coupled evolution of the dark matter and gas, which together constitute the dominant contribution to the cluster mass. In its full generality, this problem is best approached by direct simulation and a variety of numerical techniques have now been developed for this purpose. Many of the techniques currently in use (including both Eulerian and Lagrangian hydrodynamics methods) have been recently compared by means of a test calculation of the formation of a cluster by hierarchical clustering in which the gas was assumed to be non-radiative (Frenk et al. , in preparation). The different simulations resolved the cluster to different degrees, but in the regions resolved by each calculation, they generally gave remarkably similar results for most cluster properties of interest.

Already the first N-body/gasdynamic simulations showed that in the non-radiative approximation, the X-ray properties of individual clusters formed in flat cold dark matter (CDM) cosmologies resemble those of real clusters in many respects (Evrard 1990b). Subsequent simulations have developed this theme further, generally with qualitatively similar conclusions (e.g. Thomas & Couchman 1992; Kang et al. 1994; Cen & Ostriker 1994, Bryan et al. 1994; Navarro, Frenk & White 1995, Owen & Villumsen 1997). Yet, it has been clear for some time, that the simulations (at least in an  $\Omega = 1$  CDM cosmology) do not reproduce important systematic trends of the observed cluster *population* such as the slope of the relation between X-ray temperature and luminosity. This has led several authors to argue that effects not included in the simulations, such as cooling or preheating of the gas, must have played a role in the evolution of the cluster population (Kaiser 1986, Evrard & Henry 1991, Navarro, Frenk & White 1995). In particular, Navarro, Frenk & White (1995) showed that moderate preheating at high redshift leads to an acceptable luminosity-temperature relation without spoiling the overall agreement with the observed structure of the X-ray gas in individual clusters.

Useful insights into the evolution and systematic properties of the cluster population may also be obtained by studying scaling relations, an approach developed by Kaiser (1986; see also White & Rees 1978, and White 1982). These authors recognized that since gravity has no preferred scales, cluster properties determined primarily by gravity (or by other scale-free processes such as pressure gradients or hydrodynamical shocks) should obey simple scaling relations. Kaiser derived these for a population of clusters formed by hierarchical clustering from power-law initial density fluctuations in an Einstein-de Sitter universe. He concluded that, for most power spectra of interest, the cluster X-ray luminosity function evolves with redshift in the opposite sense to that indicated by the data available at the time (Edge et al. 1990, Gioia et al. 1990). More recent data, however, appear to be consistent with little or no evolution in

the cluster X-ray luminosity function out to  $z \simeq 0.3$  (Nichol et al. 1997, Rosati et al. 1998).

In this paper, we carry out a detailed investigation of the evolution of clusters in a low-density,  $\Omega_0 = 0.3$ , CDM universe. We impose the flat geometry required by inflation by setting the cosmological constant  $\Lambda_0 = 0.7$ <sup>4</sup>. We perform a set of N-body-hydrodynamical simulations of cluster formation in this cosmology. We also generalize Kaiser’s scaling laws to the case of an arbitrary cosmology and generic density fluctuation spectra. Cluster evolution in low-density universes has been explored numerically in a few previous papers (Cen & Ostriker 1994; Evrard, Metzler & Navarro 1996), but none has yet addressed in detail the evolutionary properties of the X-ray emission from individual clusters. Our extension of Kaiser’s scaling laws is based on recent numerical results by Navarro, Frenk & White (1995, 1996, 1997, hereafter NFW95, NFW96, and NFW97, respectively), who found that virialized systems formed by hierarchical clustering exhibit a remarkable structural similarity. Throughout this paper we make the simplifying assumption that only gravity, pressure gradients and hydrodynamical shocks are important in the evolution of clusters.

The plan of this paper is as follows. In §2 we derive generalized scaling laws describing correlations between various cluster properties and their redshift evolution. In §3, we describe our numerical methods and provide details of the ten clusters which we have resimulated at high resolution. These span a range of formation histories and dynamical states. Our main numerical results are presented in §4 where we investigate the structure of the dark matter and gas in our clusters, the accuracy of cluster mass estimates, the evolution of their baryon fraction and the origin of possible deviations from a universal mean baryon fraction. In this section we also carry out a comparison with the generalized scaling laws derived in §2. In §5 we compare our results with previous numerical work and with observations. A summary of our main conclusions is given in §6.

## 2. Scaling Laws

In an Einstein-de Sitter ( $\Omega = 1$ ) universe with a power-law spectrum of primordial density fluctuations,  $P(k) \propto k^n$ , the characteristic clustering mass evolves as  $M^* \propto (1+z)^{-6/(3+n)}$ . Since there are no other scales in the problem, the characteristic density of an  $M^*$  cluster can only be proportional to the density of the universe,  $\rho^* \propto (1+z)^3$ . A characteristic mass and density define, through the virial theorem, a characteristic temperature (or velocity dispersion) which scales as  $T^* \propto \sigma^{*2} \propto (1+z)^{(n-1)/(n+3)}$ . Assuming that the X-ray emission from intracluster gas is dominated by bremsstrahlung, the characteristic X-ray luminosity then scales as  $L_X^* \propto M^* \rho^* T^{*1/2} \propto (1+z)^{(7n+5)/(2n+6)}$ . The X-ray luminosity of a *typical* cluster may thus increase or decrease with redshift, depending on whether  $n$  is larger or smaller than  $-5/7$ , respectively.

These scaling relations predict the time evolution of a *typical* cluster (ie. a cluster with mass equal to the characteristic clustering mass), but they do not describe the evolution of individual clusters or the mass dependence, at fixed redshift, of the X-ray luminosity or other cluster properties. Without this information, which depends on the *internal structure* of clusters, it is not possible to assess the cosmological significance of observed correlations such as the luminosity-temperature relation or their evolution.

The simplest model assumes that: (i) the internal structure of clusters of different mass is similar;

---

<sup>4</sup>Throughout this paper we write the cosmological constant  $\Lambda$  in units of  $3H^2$ , so that a universe with  $\Omega + \Lambda = 1$  has a flat geometry. The present value of Hubble’s constant,  $H_0 = H(z=0)$ , is parameterized by  $H_0 = 100 h \text{ km s}^{-1} \text{ Mpc}^{-1}$ .

(ii) all clusters identified at some redshift have the same characteristic density; and (iii) this characteristic density scales like the mean density of the universe, ie. as  $(1+z)^3$  (see Evrard 1990b, Evrard & Henry 1991, NFW95). With these assumptions, and the further hypothesis that the relative distributions of gas and mass are similar in all clusters, it is possible to derive scaling relations between mass, luminosity, and temperature (velocity dispersion). In particular, we have that

$$T(M, z) \propto M^{2/3}(1+z), \quad (1)$$

and, assuming again that bremsstrahlung is the main emission mechanism,  $L_X \propto M\rho T^{1/2}$ , so that

$$L_X(M, z) \propto M^{4/3}(1+z)^{7/2} \propto T^2(1+z)^{3/2}. \quad (2)$$

Thus, in this model, clusters of a given temperature or mass are expected to become more luminous at higher redshifts, a useful prediction that can be tested observationally. We shall come back to this issue in §5.2.

As mentioned above, this approach has some support from recent N-body work, which shows that indeed the structure of clusters formed through hierarchical clustering exhibit a remarkable similarity (NFW96, NFW97). Regardless of cluster mass, power spectrum shape, or the value of the cosmological parameters, the density profiles of dark halos formed through hierarchical clustering can be fitted accurately by scaling a simple formula,

$$\frac{\rho_{\text{DM}}(r)}{\rho_{\text{crit}}} = \frac{\delta_c}{(r/r_s)(1+r/r_s)^2}. \quad (3)$$

Here  $\delta_c$  is a characteristic dimensionless density and  $r_s$  is a scale radius related to the total mass of the system. NFW96 and NFW97 show that these two parameters are correlated, a relation that reflects the different collapse redshift of systems of different mass. These authors also provide the necessary formulae to compute  $\delta_c$  as a function of mass in any hierarchically clustering cosmogony. We note that assuming a common characteristic density for all clusters, as in (ii) above, is equivalent to setting  $\delta_c = \text{const.}$  in eq.(3).

We show below (§4.3) that the spherical top-hat model provides a useful definition of the mass contained within the virialized region of a system (Eke et al. 1996). The virial mass,  $M_{\text{vir}}$ , is defined to be the mass contained within the radius,  $r_{\text{vir}}$ , that encloses a density contrast  $\Delta_c$ :  $M_{\text{vir}} = (4\pi\Delta_c/3)\rho_{\text{crit}}r_{\text{vir}}^3$ <sup>5</sup>. This density contrast depends on the value of  $\Omega$  and can be approximated by (Lacey & Cole 1993, Eke, Cole & Frenk 1996):

$$\Delta_c(\Omega, \Lambda) = 178 \begin{cases} \Omega^{0.30}, & \text{if } \Lambda = 0; \\ \Omega^{0.45}, & \text{if } \Omega + \Lambda = 1. \end{cases} \quad (4)$$

This formula is accurate to within 5% for  $0.15 < \Omega < 1$ . It is straightforward to show that, with this definition, the ratio between virial and scale radii, which we denote by the ‘concentration’,  $c = r_{\text{vir}}/r_s$ , is uniquely related to  $\delta_c$  by

$$\delta_c = \frac{\Delta_c}{3} \frac{c^3}{[\ln(1+c) - c/(1+c)]}. \quad (5)$$

The structure of a halo of mass  $M_{\text{vir}}$  is then completely specified by a single parameter, which may be chosen to be the characteristic density,  $\delta_c$ , or the concentration,  $c$ .

---

<sup>5</sup>We shall use ‘density contrast’ to refer to densities expressed in units of the critical density,  $\rho_{\text{crit}}(z) = 3H(z)^2/8\pi G$ , where  $H(z)$  is the current value of Hubble’s constant. The term ‘overdensity’ will be used to refer to densities in units of the mean background matter density.

We can use these results to calculate the expected interdependence of mass, temperature, and X-ray luminosity in various cosmologies. The bolometric X-ray luminosity is given by

$$L_X = \int_V \left( \frac{\rho_{\text{gas}}}{\mu m_p} \right)^2 \Lambda_c(T) dV, \quad (6)$$

where  $\Lambda_c(T)$  is the cooling function and  $\rho_{\text{gas}}(r)$  is the gas density distribution. Assuming that the gas distribution traces the dark matter, ie.  $\rho_{\text{gas}}(r) = f_{\text{gas}} \rho(r) \propto \rho_{\text{DM}}(r)$ , ( $f_{\text{gas}}$  is the gas mass fraction) and that the gas is isothermal, we find,

$$L_X = \left( \frac{f_{\text{gas}}}{3\mu m_p} \right)^2 \Delta_c F(c) M_{\text{vir}} \rho_{\text{crit}} \Lambda_c(T), \quad (7)$$

where  $F(c)$  is a function only of the concentration,

$$F(c) = c^3 \frac{1 - (1+c)^{-3}}{[\ln(1+c) - c/(1+c)]^2}. \quad (8)$$

Note that if gas traces mass the X-ray luminosity converges, since  $\rho_{\text{gas}} \propto r^{-1}$  near the center. Eq.(7) expresses the luminosity in terms of the mass, temperature and concentration of the system. The same dependence of  $L_X$  on  $M$  and  $T$  (but different proportionality constants) is expected even if the gas distribution does not trace mass in detail, so long as the gas density can be written as  $\rho_{\text{gas}}(r) = \Theta(r/r_s) \rho_{\text{DM}}(r)$ , with the same dimensionless function  $\Theta(r/r_s)$  for all clusters.

In order to derive the luminosity-temperature relation, we need a relationship between mass and temperature or, equivalently, between mass and velocity dispersion. The existence of a characteristic density in the structure of the system implies the existence of a characteristic velocity as well. This is easily seen in the circular velocity profile,  $V_c(r) = (GM(r)/r)^{1/2}$ , implied by eq.(3),

$$\left( \frac{V_c(r)}{V_{\text{vir}}} \right)^2 = \frac{1}{x} \frac{\ln(1+cx) - (cx)/(1+cx)}{\ln(1+c) - c/(1+c)}. \quad (9)$$

Here  $V_{\text{vir}} = (GM_{\text{vir}}/r_{\text{vir}})^{1/2}$  is the circular velocity at the virial radius, and  $x = r/r_{\text{vir}}$  is the radius in units of  $r_{\text{vir}}$ . From eq.(9),  $V_c(r)$  has a maximum,  $V_{\text{max}}$ , at  $r \approx 2r_{\text{vir}}/c$ ,

$$V_{\text{max}}^2 \approx V_{\text{vir}}^2 \frac{0.22 c}{\ln(1+c) - c/(1+c)}. \quad (10)$$

This maximum circular velocity is independent of the definition of virial radius, and may be taken to represent the characteristic velocity of the system. Other measures of the depth of the potential well, such as the velocity dispersion of the dark matter,  $\sigma_{\text{DM}}$ , are expected to scale with  $V_{\text{max}}$ . In the absence of non-gravitational heating or cooling effects, the characteristic temperature of the gas should also scale as  $T \propto V_{\text{max}}^2$ , so that

$$T \propto \sigma_{\text{DM}}^2 \propto V_{\text{max}}^2 \propto V_{\text{vir}}^2 \frac{c}{[\ln(1+c) - c/(1+c)]}, \quad (11)$$

or

$$T \propto \sigma_{\text{DM}}^2 \propto \left( \frac{\Delta_c}{\Omega} \right)^{1/3} H(c) M_{\text{vir}}^{2/3} (1+z), \quad (12)$$

where  $H(c) \equiv c/[\ln(1+c) - c/(1+c)]$  and we have used  $\rho_{\text{crit}}(z) \propto (1+z)^3/\Omega(z)$ . These relations (eqs. 7 and 12) can be used to construct the luminosity-temperature relation. Assuming that the main emission process is bremsstrahlung,  $\Lambda_c(T) \propto T^{1/2}$ , we can write eq.(7) as,

$$L_X \propto f_{\text{gas}}^2 \Delta_c F(c) M_{\text{vir}} \rho_{\text{crit}} T^{1/2} \quad (13)$$

which, using eq.(12), may be expressed as,

$$L_X \propto f_{\text{gas}}^2 \left( \frac{\Delta_c}{\Omega} \right)^{1/2} \frac{F(c)}{H(c)^{3/2}} T^2 (1+z)^{3/2}. \quad (14)$$

These relations generalize the expected dependence between luminosity, mass and temperature to arbitrary values of  $\Omega$  and arbitrary (ie. non power-law) power spectra. Comparing eqs. (1) and (2) with (12) and (14) we see that, except for the functions of  $c$ , the generalized relations are identical to those derived assuming a common characteristic density for all clusters. Indeed, for  $\Omega = 1$  and  $c = \text{const.}$ , these equations are identical. Eqs.(12) and (14) require the value of the concentration as a function of mass, power spectrum, and cosmological parameters. A simple algorithm to calculate this is given in the Appendix of NFW97.

### 3. Numerical Method

#### 3.1. Initial conditions

A large N-body simulation of an  $\Omega_0 = 0.3$ ,  $\Lambda_0 = 0.7$ ,  $h = 0.7$ , CDM cosmogony was carried out using the AP<sup>3</sup>M code written by Couchman (1995). The power spectrum used is that of Bond & Efstathiou (1984). This simulation followed  $64^3$  particles in a cube of side  $180 h^{-1} \text{Mpc}$ . Gravitational accelerations were computed using a parent mesh of  $128^3$  grid cells, and softened with an effective Plummer comoving lengthscale of  $14 h^{-1} \text{kpc}$ . The simulation was stopped after 26 expansion factors when  $\sigma_8$ , the linear theory *rms* mass fluctuation on spheres of  $8 h^{-1} \text{Mpc}$ , was equal to 1.05. We identify this epoch with the present, consistent with both the standard COBE normalization and the observed abundance of rich clusters (White et al 1993).

We then applied a ‘spherical overdensity’ group-finding algorithm (Lacey & Cole 1994) on this final configuration in order to identify clumps with a mean interior density contrast of  $\Delta_c \sim 100$ , which corresponds to the ‘virial’ radius in the spherical top-hat model for  $\Omega_0 = 0.3$  (see eq.4). The ten most massive clusters were selected from this list and all of their particles within about  $2 r_{\text{vir}}$  were identified. No attempt was made to cull the list for the presence of massive neighbors or for the dynamical state of the cluster. Some of our selected clusters are in the process of merging, and essentially all of them show, to some degree, signs of recent accretion and departures from equilibrium. Figure 1 shows, at  $z = 0$ , the positions of these clusters in projection within the original box. Each cluster is surrounded with a circle of radius  $1.5 r_{\text{vir}}$  (only particles within  $r_{\text{vir}}$  are shown) and is labeled in decreasing order of mass. The ten clusters span a factor of  $\sim 3$  in mass, with a mean of  $\sim 10^{15} M_{\odot}/h$ , and typically have  $\sim 1000$  particles each.

#### 3.2. High-resolution resimulations

For each cluster, all particles identified within  $\sim 2 r_{\text{vir}}$  were traced back to the initial conditions, where a small box containing all of them was drawn. These particles were then replaced with equal numbers of gas and dark matter particles on a cubic grid which was then perturbed using the waves of the original AP<sup>3</sup>M simulation, together with extra high-frequency waves added to fill out the power spectrum between the Nyquist frequencies of the old and new particle grids. The number of ‘high-resolution particles’ was varied as a function of the size of the small box and of the mass of each cluster so as to have, at  $z = 0$ , about the same number of particles in each cluster. All remaining material in the large simulation was coarse-sampled and replaced by approximately 10,000 dark matter particles of radially increasing mass.

We list the relevant numerical parameters in Table 1. The first four columns give: (1) a label for the run, (2) the size of the ‘high-resolution’ box in comoving  $h^{-1}\text{Mpc}$ , (3) the number of gas particles (or dark matter particles, since they are the same) loaded into this region, and (4) the mass of each gas particle, which is assigned assuming an overall gas mass fraction of 10%. This is consistent with the universal baryon fraction suggested by the primordial abundance of the light elements,  $\Omega_b/\Omega_0 \sim 0.015 h^{-2}/0.3 \approx 0.1$  (Copi, Schramm & Turner 1995). The mass of each dark matter particle is therefore nine times that of a gas particle. (We note that, since radiative cooling is neglected in the simulations, all our results may be rescaled to arbitrary values of the gas fraction, so long as the gas mass remains a small fraction of the total.) In order to ensure that hydrodynamical forces do not play a significant role in the evolution of the gas until the collapse of the first resolved structures, we initially assign a very low internal energy to each gas particle, corresponding to a temperature of about  $\sim 15\text{ K}$ .

### 3.3. The Code

We use the N-body/Smooth Particle Hydrodynamics (SPH) code described in detail by Navarro & White (1993), modified as follows: (i) The code has been adapted to run in a  $\Lambda \neq 0$  universe by the addition of a centrally symmetric acceleration directed outwards, of magnitude proportional to the distance of each particle to the center. (ii) The program computes the gravitational accelerations using a GRAPE-3Af board. The neighbor lists needed for the SPH computations are also retrieved from the GRAPE and processed in the front-end workstation. The implementation of these modifications is straightforward and very similar to those described by Steinmetz (1996), where the reader may find further details.

The effects of radiative cooling, heating by a photoionizing UV background, or star formation can be handled by this code but were neglected in the simulations presented here. The only physical processes included are gravity, pressure gradients, and hydrodynamical shocks. An ideal gas equation of state with  $\gamma = 5/3$  is used to relate pressure and internal energy. Details and tests of our SPH implementation may be found in Navarro & White (1993).

Gravitational accelerations are softened using a *physical* (not comoving) Plummer scale-length of  $14 h^{-1}\text{ kpc}$ . This is less than 1% of the final virial radius of all ten clusters. All simulations were started at  $z = 25$  and integrated to  $z = 0$  using individually adjusting timesteps for each particle. Typically, timesteps ranged between  $\sim 10^6$  and  $\sim 10^9$  yrs, depending on the dynamical situation experienced by each particle.

### 3.4. Units and numerical estimators

#### 3.4.1. X-ray luminosity

We follow NFW95, and use the following estimator for the *bolometric* X-ray luminosity of a cluster,

$$L_X = 1.2 \times 10^{-24} \left( \frac{m_{\text{gas}}}{\mu m_p} \right) \sum_{i=1}^{N_{\text{gas}}} \frac{\rho_i}{\mu m_p} \left( \frac{kT_i}{\text{keV}} \right)^{1/2} \text{ erg s}^{-1}, \quad (15)$$

where  $m_p$  is the proton mass,  $\mu = 0.6$  is the mean molecular weight of a primordial plasma,  $m_{\text{gas}}$  is the mass of a gas particle, and  $\rho_i$  and  $T_i$  are the density and temperature at the location of particle  $i$ , respectively. Masses and densities are in cgs units in this formula, which assumes that the main X-ray emission mechanism is bremsstrahlung, ie.  $\Lambda_c(T) = 1.2 \times 10^{-24} (kT/\text{keV})^{1/2} \text{ erg cm}^3 \text{ s}^{-1}$ . The sum is

carried out over all gas particles within the virial radius of a cluster. Unless otherwise specified, we shall quote luminosities in units of  $h^{-2}$  erg s $^{-1}$  (1 erg =  $10^{-7}$  Joules). Luminosities depend on the value assumed for the gas fraction,  $f_{\text{gas}} = 0.1$ , but can be rescaled to other values by  $f_{\text{gas}}^2$ .

### 3.4.2. Entropy

The entropy per particle is defined as  $s_i = \ln(kT_i/\rho_i^{2/3}) + 6$ , where  $kT_i$  is expressed in keV and  $\rho_i$  in units of  $10^{10}h^2M_\odot/\text{Mpc}^3$ . (The factor 6 is an arbitrary constant.) In the case of dark matter particles,  $\rho_i$  is the mean dark matter density within a sphere centered on  $i$  containing the 30 nearest dark matter particles, and  $kT_i = \mu m_p \sigma_i^2$ , where  $\sigma_i$  is the 1D velocity dispersion of the particles.

## 4. Results

Table 2 summarizes the bulk properties of the ten clusters at  $z = 0$ . All quantities are computed within the virial radius. The majority of clusters have more than  $10^4$  dark matter particles within the virial radius, except cl07a and cl08a, which have significantly fewer. This is a result of their physical proximity at  $z = 0$  (see Figure 1) which demands a large high-resolution box in order to enclose all the material that ends up within  $2r_{\text{vir}}$  of the center, and consequently a larger mass per particle if we are limited to  $N_{\text{gas}}^{\text{tot}} < 40^3$ , the maximum number we can afford to run.

Particle plots of the gas and dark matter configurations of three clusters at  $z = 0$  are shown in Figure 2. The gas appears to be slightly more spherical than the dark matter because it traces the equipotentials of the system, which are significantly rounder than the dark matter density distribution (Evrard 1990a). The dark matter retains more small scale structure than the gas. This is presumably a result of the combined effects of ram-pressure stripping of gas as small clumps move in the hot atmosphere of the main cluster, and of numerical limitations which tend to smooth the gas distribution on mass scales smaller than  $\sim 50$  particles.

### 4.1. Evolution of cluster bulk properties

The evolution of all clusters is similar to that described in previous work (see, eg., §3.1 of NFW95), and is illustrated in Figure 3 for cluster cl01a. A cluster accretes most of its final mass in the form of mergers with smaller clumps which flow along large-scale filaments easily noticeable in this figure. Figures 4 and 5 show the evolution of the bulk properties of each cluster: mass, velocity dispersion, temperature, X-ray luminosity, central entropy (see figure label), and ‘beta’-parameters. The latter are defined below in eqs.(18) and (19). All these properties are measured within the current virial radius of the most massive progenitor of the final system.

As is clear from Figures 4 and 5, clusters form late, accreting on average half of their final mass since  $z \sim 0.5$ . This is shown quantitatively in Table 1, which lists the ‘formation redshift’, of each cluster,  $z_{1/2}$ , defined as the epoch when the mass of the most massive progenitor first exceeds one-half of the mass of the system at  $z = 0$ . The formation redshifts are in good agreement with analytical estimates based on the Press-Schechter theory (Lacey & Cole 1993). Note the large scatter in  $z_{1/2}$ , which varies between  $\sim 0.9$  and  $\sim 0.2$  as a result of the intrinsic variety of formation histories of individual clusters.



The evolution of our ten clusters is summarized in Figure 6 where we plot the average, over all clusters and at each time, of the bulk properties scaled to their value at  $z = 0$ . As clusters grow increasingly massive, the potential well deepens, and they become hotter and more luminous in X-rays. Although the mass increases rapidly with time, other cluster properties evolve more slowly. At  $z \sim 1$  clusters are, on average, four times less massive and about half as luminous or as hot as at  $z = 0$ . Cluster masses double after  $z \sim 0.5$ , but their luminosities and temperatures increase only by 20%. The velocity dispersion changes even less since it scales like the square-root of the temperature. Therefore, in this cosmogony we expect distant luminous clusters to be almost as bright and as hot as those in the local universe.

The evolution is punctuated by mergers during which clusters may brighten temporarily by more than a factor of two (c.f. Figures 4 and 5). The central ‘entropy’ of the gas and dark matter (see §3.4.2) also increases steadily, and by roughly similar amounts, as the cluster evolves. This suggests similarity in the evolution of gas and dark matter, conforming to the hypothesis on which we based our derivation of scaling laws in §2.

These results may be compared with the predictions of the scaling laws derived in §2. The thick dashed lines in Figure 6 show the evolution of  $T$ ,  $\sigma_{\text{DM}}$ , and  $L_X$  predicted by eqs.(12) and (14) for a cluster of mass equal to the mean plotted in the upper left panel. All curves are normalized to the values of each quantity at  $z = 0$ . Concentrations are computed using the algorithm given in the Appendix of NFW97.

The agreement between the predictions of the scaling laws and the results of the simulations is remarkable, and implies that the gas and dark matter components evolve similarly as clusters grow more massive. The structure of the gas and dark matter within clusters must therefore remain either similar or proportional to one another at all times, an issue we investigate further below. Appropriate scaling behaviour is widely regarded as a powerful test of numerical techniques. The agreement between our simulations and the scaling laws provides a convincing validation of the Smooth Particle Hydrodynamics technique we are using here.

## 4.2. Cluster structure

Figures 7 and 8 illustrate the structure of our clusters at  $z = 0$ . Many of them seem to be close to equilibrium, with the exception of cl04a, cl05a, cl08a, and cl09a. Departures from equilibrium show up clearly in the ratio of the gas bulk kinetic to thermal energies, shown in the fourth row of Figures 7 and 8. This ratio would be zero, of course, if the gas were in perfect hydrostatic equilibrium, but it is temporarily different from zero as a result of recent accretion. Table 2 lists the average values of this ratio within the virial radius. Ongoing merger events are also easy to spot in the mean radial velocity profiles, which show significant departures from the zero mean characteristic of a system in virial equilibrium. Thus, even in this low-density universe, 4 out of 10 clusters are substantially out of equilibrium, a large fraction which may hamper attempts to determine the cosmological parameters from the fraction of relaxed, virialized clusters (Mohr, Evrard & Fabricant 1995).

In all clusters, and almost regardless of how close to equilibrium they are, the velocity distribution of the dark matter is radially biased, albeit mildly;  $\beta_{\text{an}} = 1 - \bar{v}_t^2/2\bar{v}_r^2 \approx 0.2$ , with a weak radial dependence (see bottom row of Figures 7 and 8). This is more easily seen in the average velocity anisotropy profile shown in the lower right panel of Figure 9. Outside a small inner region where the velocity distribution is very nearly isotropic, the magnitude of the radial bias is essentially constant at  $\beta_{\text{an}} = 0.2$  out to  $r = (1/2)r_{\text{vir}}$ ; beyond that radius the bias increases, peaking at about  $\beta_{\text{an}} \approx 0.4$  at the virial radius. This radial behaviour can be

approximated as  $\beta_{an} = 0.15 + 0.2(r/r_{\text{vir}})$ . Similar results have been reported in previous work (eg., Evrard 1990b, Cole & Lacey 1996).

The average gas temperature profile is shown in the upper left panel of Figure 9 as a dashed line. To form this average, individual temperatures were scaled to the ‘virial temperature’ of each system, defined as

$$kT_{\text{vir}} = \frac{1}{2}\mu m_p V_{\text{vir}}^2 = \frac{1}{2}\mu m_p \frac{GM_{\text{vir}}}{r_{\text{vir}}}. \quad (16)$$

As found by Evrard (1990b) and NFW95, the gas near the center is close to isothermal; its temperature at  $r = (1/3)r_{\text{vir}}$  differs from the central one by less than 25%. Beyond that radius, the temperature drops faster, approximately as  $T \propto r^{-1/2}$ , reaching about half the central value at the virial radius. The dark matter ‘temperature’ (ie. the square of the velocity dispersion about the mean in each radial shell normalized to  $V_{\text{vir}}$ ) has a similar behaviour, but drops below the gas temperature near the center. This is a direct consequence of the different density profiles of gas and dark matter in the inner regions. As may be seen in Figures 7 and 8, the gas is less centrally concentrated than the dark matter and must therefore be hotter in order to be in equilibrium within the same gravitational potential.

The lower left panel in Figure 9 shows the average cumulative X-ray luminosity profile. The density profiles are rather peaked and, as a result, the luminosity is very concentrated; half the total energy is generated within 10% of the virial radius. Thus, most of the emission comes from the region where the gas is nearly isothermal. Any significant departures from isothermality observed near the center of X-ray clusters will most likely signal ongoing accretion/merger events or the presence of cooling flows.

### 4.3. Applicability of the spherical top-hat model

In the spherical top-hat model, the density of a virialized system is estimated by assuming that, at the time of collapse, the system has an equilibrium radius equal to approximately one-half of its turnaround radius. This virialized density contrast,  $\Delta_c$ , can be computed analytically and depends on the values of  $\Omega$  and  $\Lambda$  at the time of collapse, as given in eq.(4) (see Lacey & Cole 1993, and Eke et al 1996 for derivations).

As explained in §2, we have used this density contrast to guide our choice of the radius,  $r_{\text{vir}}$ , that encloses the virialized mass of a cluster. How well does this definition work? We illustrate the situation in the left panels of Figure 10 which show the mean radial velocity profiles at three different redshifts, averaged over the ten clusters. Solid and dashed lines represent dark matter and gas components, respectively. These panels show three different regions easily identifiable in each system: (i) an inner region where the system is close to virial equilibrium, ie.  $\langle v_{\text{rad}} \rangle \approx 0$ ; (ii) a region dominated by infall,  $\langle v_{\text{rad}} \rangle < 0$ ; and (iii) an outer region where radial shells are still expanding away from the system,  $\langle v_{\text{rad}} \rangle > 0$ . The virialized region extends out to  $r \approx r_{\text{vir}}$  in all cases. This supports our choice of  $r_{\text{vir}}$  for characterizing the virialized mass of a system.

At  $z = 0, 0.38$ , and  $1.09$  this definition of virial radius corresponds to density contrasts of 97, 130, and 160, which correspond to *overdensities* of 324, 245, and 200, respectively. Our results are therefore consistent with those of Crone, Evrard & Richstone (1994) who found that, at overdensities of order  $\sim 300$  or higher, clusters were close to hydrostatic equilibrium. Figure 10 also shows that alternative definitions of the ‘virial’ radius work reasonably well so long as they are referred to some specified density contrast. For example, the radius,  $r_{200}$ , corresponding to density contrast  $\Delta_c = 200$ , used by NFW97 (vertical dotted lines to the left of  $r = r_{\text{vir}}$ ), or the radius where the circular orbit timescale equals the current age of

the universe (vertical dotted lines to the right of  $r = r_{\text{vir}}$ ) also describe the virialized region of a cluster relatively well.

#### 4.4. Density profiles

The second row in Figures 7 and 8 shows the density profiles of the gas and dark matter components at  $z = 0$ , scaled to the mean background density; the radius is scaled to the virial radius in each case. As discussed by NFW95 (see also Crone et al 1994), these scaled profiles look very similar, regardless of cluster mass. Average profiles at  $z = 0, 0.38$ , and  $1.09$  are shown in the right-hand panels of Figure 10. Error bars indicate the standard deviation in the overdensity at each radius, computed using the ten most massive progenitors present at each redshift. A vertical arrow indicates the value of the gravitational softening.

The fits to the dark matter profiles are obtained using eq.(3). This formula clearly describes very well the dark matter profiles over about two decades in radius, from the gravitational softening out to the virial radius. Near the center, the dark matter density increases monotonically inwards, and there is no indication that it approaches a well defined central value except for that imposed by the gravitational softening and the finite number of particles.

The parameters of the fits are listed in Table 3. These parameters may be compared with the predictions of NFW97, who found that the characteristic density,  $\delta_c$  (or, equivalently, the concentration,  $c$ ), is directly proportional to the mean density of the universe at the time of assembly of each system. Following the procedure outlined in the Appendix of their paper we computed the concentrations expected for clusters identified at  $z = 0$  and at  $z = 1.09$  in this particular cosmogony. The results are shown as solid ( $z = 0$ ) and dashed ( $z = 1.09$ ) lines in the upper panel of Figure 11. There is no free rescaling allowed in this comparison, so the agreement at  $z = 0$  (open squares) is impressive, especially because the concentrations derived analytically are expected to apply mainly to clusters near equilibrium, and not necessarily to an ensemble of systems chosen at random stages of evolution.

According to the analytical procedure, at fixed mass the concentration is expected to *decrease* with increasing redshift. The same effect, although slightly more pronounced, is seen in the simulations. At  $z = 1.09$ , the predicted concentration is about  $\sim 40\%$  larger than in the simulated clusters. This discrepancy is most likely the result of numerical limitations, since at  $z \approx 1$  clusters are not as well resolved as at  $z = 0$ . They contain  $\sim 5$  times fewer particles, and the gravitational softening is about 2% of the virial radius, compared with  $\sim 0.7\%$  of  $r_{\text{vir}}$  at  $z = 0$ . It is therefore likely that the dark matter concentration has been underestimated at  $z \sim 1$  because of these effects.

We have tested this directly by both increasing and decreasing (by factors of  $\sim 2$ ) the number of particles in three of the runs (*cl01a*, *cl09a*, and *cl10a*). These extra runs were evolved until  $z = 1.09$ , and the dark matter concentration parameter was computed using the same procedure as before. The results are shown with connected starred symbols in the upper panel of Figure 11. As the number of particles increases so does the concentration. The highest resolution runs have 5,000-10,000 particles within the virial radius, and in this case there is little difference between predicted and numerically determined concentrations.

The density profile of the gas component differs significantly from the dark matter (see Figure 10). The gas is less centrally concentrated, and, near the center, a well defined, constant density region (a ‘core’) is clearly apparent. This core extends beyond the region likely to be compromised by numerical limitations (ie. the gravitational softening), especially at  $z = 0$ , when the clusters are best resolved. Fits

using eq.(3) give unacceptably large values of  $\chi^2$ , so we decided instead to fit the gas profiles using the  $\beta$ -model (Cavaliere & Fusco-Femiano 1976), traditionally used to fit X-ray data:

$$\frac{\rho_{\text{gas}}}{\rho_{\text{crit}}} = \delta_0 \left(1 + (r/r_{\text{core}})^2\right)^{-3\beta_{\text{fit}}/2}. \quad (17)$$

This formula provides a good description of the gas profiles at all redshifts, as may be seen in Figure 10. The typical core radius is about  $100 h^{-1}$  kpc at  $z = 0$  (Table 3), in good agreement with observations (eg. Jones & Forman 1984). On average, 50% of the total X-ray luminosity originates within  $\sim 2 r_{\text{core}}$ . Clusters are, on average, less massive (and smaller) at high-redshift, so their core radii are expected to be smaller as well, by about a factor of two at  $z \sim 1$ . This expectation could, in principle, be tested against observations when accurate estimates of core radii at modest-to-high redshifts become available.

If the gas and dark matter density profiles are not identical, but clusters evolve approximately as predicted by the scaling laws (see Figure 6), then the profiles must remain proportional to each other, independently of cluster mass or redshift. That this is indeed the case may be seen by examining the fit parameters listed in Table 3. The ratio of the gas core radius to the dark matter scale radius,  $r_{\text{core}}/r_s \sim 0.33$ , remains approximately constant since  $z = 1$ , as does the ratio of characteristic densities,  $\delta_0/\delta_c \sim 0.29$ .

Why are the radial profiles of the gas and dark matter different but nevertheless remain proportional to each other? Inspection of Figures 6 and 10 suggest that the explanation lies in the evolution of the net central entropy of the two components shown in the bottom left panel of Figure 6. By construction, at very early times (the initial conditions) the specific entropy of gas and dark matter is the same, but the entropy gain is different during the assembly of the first virialized structures. At later times the entropy gain is such that the ratio between gas and dark matter central entropies remains approximately constant.

This difference has been noted and studied by Navarro & White (1993), Pearce, Thomas & Couchman (1994) and NFW95, and occurs as a result of the different behavior of collisional and collisionless fluids during mergers. Since gas is stopped in shocks while the dark matter in merging subsystems can mix freely, the gas tends to ‘lag behind’ during the assembly of the system, creating an effective phase difference that results in a net transfer of energy (and entropy) from the dark matter to the gas. Thus in each merger event the gas and dark matter raise their entropies by different amounts. Assuming that the central entropy gain of each component per merger event is always  $\Delta s^{\text{gas}}$  and  $\Delta s^{\text{DM}}$  for the gas and dark matter, respectively, the ratio between final entropies will tend to a constant,  $\Delta s^{\text{gas}}/\Delta s^{\text{DM}}$ , as soon as the current entropy exceeds significantly the initial value. Since the initial entropy is negligible, soon after the collapse and virialization of the first resolved clumps the gas and dark matter settle to equilibrium configurations that are not identical but which remain proportional to each other at all times.

Finally, since the gas distribution is effectively determined by that of the dark matter, limited numerical resolution can affect the gas central properties, and in particular estimates of the X-ray luminosity. This is shown in the lower panel of Figure 11, where we show how the X-ray luminosity depends on particle number for the convergence tests described above. X-ray luminosities,  $L_X$ , are normalized to  $L_X^{\text{exp}}$ , the value expected from the scaling laws described in §2 (see dashed line in upper left panel of Figure 13). Clearly, more than about 3,000-5,000 gas particles within the virial radius are needed in order to obtain convergent values of  $L_X$ . We shall come back to this issue in §4.6.

#### 4.5. Cluster baryon fraction

As discussed by White et al (1993), the mean baryonic mass fraction within the virial radius of a cluster is unlikely to exceed the universal baryon fraction. This is because, by definition, the virial radius separates the virialized region of the system from the region where shells of material are infalling for the first time. Measurements of the baryon fraction in clusters can therefore be compared with independent estimates of the universal mean,  $\Omega_b/\Omega_0$ , from, for example, Big Bang nucleosynthesis models, in order to constrain the value of the density parameter  $\Omega_0$ . This theoretical argument has led to significant interest in measurements of the baryon fraction in clusters (David, Jones & Forman 1995, White & Fabian 1995, Loewenstein & Mushotzky 1996, Gunn & Thomas 1996, Evrard 1997) and to renewed theoretical and observational efforts to estimate  $\Omega_b$  as accurately as possible (Steigmann & Tosi 1995; Copi et al. 1995; Rugers & Hogan 1996; Tytler, Fan & Burles 1996; Songaila, Wampler & Cowie 1997). Our simulations allow us to quantify possible biases in the cluster baryon fraction relative to the global mean.

The cumulative gas (baryon) fraction,  $f_{gas}^c$ , for all ten simulated clusters at  $z = 0$  is shown as a function of radius in Figure 12. This fraction is expressed in units of the universal value ( $\Omega_b/\Omega_0 = 0.1$ ) assumed in the simulations. The gas fraction increases with radius because the gas distribution is less centrally concentrated than the dark matter distribution (cf. §4.4). At  $z = 0$ , the gas fraction within  $r_{vir}$  is 85-90% of the universal value but, within one gas core radius ( $\sim 5$ -10% of the virial radius; see Table 3), it can be as low as 50% of  $\Omega_b/\Omega_0$ . Within  $r_{core}$ , large variations, ranging from 20% to more than 60% of the global mean, are seen from cluster to cluster, reflecting differences in dynamical history. Only at  $r \sim 3r_{vir} \approx 6h^{-1}$  Mpc (close to the turnaround radius) do the baryon fractions converge to the universal mean.

Because gas and dark matter densities remain approximately proportional at different times (§4.4), these results are not expected to depend significantly on redshift. This is illustrated in the bottom panel of Figure 12, where we show, as a function of  $z$ , the gas fractions within 3 different radii averaged over all ten clusters. To avoid overlaps, error bars have been chosen to represent standard deviations in the mean computed from the ten systems at each redshift, ie. they are  $10^{1/2}$  times smaller than the scatter in the baryon fraction.

To summarize, our simulations indicate that within the virial radius the baryon fraction in clusters provides a measure of the universal mean which is only mildly biased low (by  $\sim 10\%$  within  $r_{vir}$ ). A similar result has been reported in most simulations published to date, and appears to be independent of cluster mass and of the values of  $\Omega_0$  or  $\Omega_b$  (Evrard 1990b; Thomas & Couchman 1992; Kang et al. 1994; Metzler & Evrard 1994; NFW95; however see Anninos & Norman 1996). The magnitude of this bias might change if additional physics are included in the simulations. For example, cooling may increase the baryon fraction near the center, while heating by non-gravitational processes acts in the opposite direction. However, even models with extreme cooling are unable to raise the baryon fraction within  $r_{vir}$  by more than 25% (White et al 1993). Similarly, extreme preheating models cannot reduce it by more than  $\sim 30\%$ , especially in rich clusters (Metzler & Evrard 1994, NFW95). It is therefore unlikely that the baryon fractions within  $r_{vir}$  differ significantly from the universal mean. On the other hand, baryon fractions within  $r \ll r_{vir}$  can vary significantly from cluster to cluster, depending on the dynamical state of the system. This calls for caution when interpreting observational results based on measurements that probe only the inner regions of clusters and do not extend to  $r \approx r_{vir}$  (see, eg., Loewenstein & Mushotzky 1996 and Evrard 1997).

#### 4.6. Comparison with analytical scaling laws

Figure 13 shows correlations between the main structural parameters of our simulated clusters: mass, velocity dispersion, X-ray luminosity, and X-ray emission-weighted temperature, as well as the redshift dependence of these correlations. Open squares correspond to clusters at  $z = 0$ , and starred symbols to progenitors identified at  $z = 1.09$ . The solid lines in each panel show the scaling relations derived in §2, at  $z = 0$ ; dashed lines illustrate the changes in slope and normalization at  $z = 1.09$  implied by the scaling laws. Specifically, we use eq.(12) for the mass-temperature relation, eq.(11) for the temperature-velocity dispersion relation, and eq.(14) for the luminosity-temperature relation.

##### 4.6.1. $T$ - $\sigma_{\text{DM}}$ relation

The zero-point in the temperature-velocity dispersion relation is fixed by the usual ‘beta’-parameter, defined by

$$\beta_{T\sigma} = \frac{\mu m_p \sigma_{\text{DM}}^2}{kT}. \quad (18)$$

The solid line in the  $T$ - $\sigma_{\text{DM}}$  panel in Figure 13 assumes  $\beta_{T\sigma} = 1$ . The upper dotted line corresponds to  $\beta_{T\sigma} = 1.25$  and the lower dotted line to  $\beta_{T\sigma} = 0.8$ . Clearly  $\beta_{T\sigma} = 1$  is a very good approximation to the results of the simulations at all times. This is illustrated further in the right-hand panels of Figure 14, where we show the distribution of  $\beta_{T\sigma}$  values at three different redshifts,  $z = 0, 0.38$ , and  $1.09$ . The mean is indistinguishable from unity, and the dispersion is rather small ( $\sim 0.13$ ). Since our sample of clusters contains systems in different evolutionary stages, this suggests that unusually large or small observed values of  $\beta_{T\sigma}$  are likely to be caused by systematic effects such as the inclusion of interlopers in the computation of the velocity dispersion, large differences between the galaxy and mass distributions, or temperature measurements affected by non-gravitational effects such as cooling flows.

##### 4.6.2. $T$ - $M_{\text{vir}}$ relation

In an analogous way, we set the zero point of the mass-temperature relation through another ‘beta’-parameter,

$$\beta_{TM} = \frac{T_{\text{vir}}}{T} = \frac{\mu m_p}{2^{4/3} kT} (GH_0 M_{\text{vir}})^{2/3} \left( \Delta_c \frac{\Omega_0}{\Omega} \right)^{1/3} (1+z). \quad (19)$$

Thus  $\beta_{TM}$  relates the ‘virial temperature’ of the system (which depends only on the virial mass, see eq. 16) to the X-ray emission-weighted temperature,  $T$ , which is accessible to observation. This parameter is crucial for relating observations to calculations that deal only with masses, such as N-body studies or analytic calculations based on the Press-Schechter theory (see, eg., Eke et al 1996). We assume  $\beta_{TM} = 1$  in the scaling relations plotted in the mass-temperature panel of Figure 13.

One drawback of this way of relating cluster mass and temperature is its dependence on our somewhat arbitrary definition of virial mass (§2), which makes no reference to the internal structure of the system. For example, two clusters with the same virial temperature (or mass) but different concentrations may have different X-ray temperatures because  $T$  traces the depth of the potential well near the center, and this depends directly on the concentration. As discussed in §2, X-ray temperatures are likely related to the characteristic (maximum) circular velocity,  $V_{\text{max}}$ , of the system rather than to the virial velocity or

temperature. Using eqs.(11), (16) and (19), we have,

$$\beta_{TM} = \frac{T_{\text{vir}}}{T} \propto \frac{1}{H(c)} = \frac{[\ln(1+c) - c/(1+c)]}{c}. \quad (20)$$

As shown in Figure 11, the average concentration of our simulated clusters increases with time, from  $c \approx 4$  at  $z \sim 1$  to  $c \approx 6.5$  at  $z = 0$ . Thus, from eq.(20) we expect  $\beta_{TM}$  to decrease by about 13% during this time interval. This expectation is in excellent agreement with the evolution reported in Table 4:  $\beta_{TM}$  decreases from 1.12 at  $z \sim 1$  to 0.98 at  $z = 0$ . This result is shown graphically in the bottom right panel of Figure 6, where the upper thick dashed line is the expected evolution of  $\beta_{TM}$  according to eq.(20) (normalized to unity at  $z = 0$ ), which should be compared to the solid line, which shows  $\beta_{TM}$  measured directly from the simulations.

Although noticeable, these changes in  $\beta_{TM}$  are small ( $\sim 10\%$ ) compared with the scatter in individual determinations at any given time ( $\sim 20\%$ ), and therefore they are unlikely to have a large effect on mass determinations based solely on X-ray temperatures (see, eg., Evrard, Metzler & Navarro 1996). The values chosen to convert masses into temperatures by Eke et al (1996) ( $\beta_{TM} = 1.00 \pm 0.10$ ) are in good agreement with these results.

#### 4.6.3. $L_X$ - $T$ and $L_X$ - $\sigma_{\text{DM}}$ relations

We normalize the luminosity-temperature relation predicted by eq. (14) by choosing the proportionality constant so that  $L_X(10 \text{ keV}) = 8.5 \times 10^{44} h^{-2} \text{ erg s}^{-1}$  at  $z = 0$ . This relation is shown as a solid line in the top left panel of Figure 13. The dashed curve is the relation expected at  $z = 1.09$  using the same proportionality constant. The normalization of the  $L_X$ - $\sigma_{\text{DM}}$  relation follows from this and from the  $T$ - $\sigma_{\text{DM}}$  relation discussed above. At  $z = 0$ , there is good agreement between the analytical and numerical results, but at  $z = 1.09$  there are some discrepancies which, as we now discuss, are almost certainly due to numerical limitations.

Figure 13 shows that, in general, the scaling laws derived in §2 describe quite well the correlations between structural properties of simulated clusters and their evolution. At a fixed temperature, for example, clusters are expected to brighten by almost a factor of two at  $z \sim 1$  compared to clusters at  $z = 0$ . Our simulated clusters are only slightly underluminous (by about  $\sim 30\%$ ) relative to this expectation. This is not entirely surprising because at  $z \sim 1$  poorer numerical resolution results in artificially low central densities, and a significant underestimation of the X-ray luminosity. Indeed, according to Figure 11 (top panel), at  $z = 1.09$  the average concentration of the simulated clusters is  $c \approx 4$ , whereas the expected concentration is almost 50% higher. Plugging these numbers into the concentration-dependent factors of eq.(14),  $F(c)/H(c)^{3/2}$ , we find that this effect alone can lead to underestimates of the total X-ray luminosity of about 35%, consistent with the deviations observed in the  $L_X$ - $T$  panel of Figure 13. Further support for this interpretation is provided by the lower panel in Figure 11, which shows that convergent X-ray luminosity estimates require more than about 3,000-5,000 gas particles within the virial radius. Most clusters have fewer gas particles than that at  $z \sim 1$ , so systematic underestimation of  $L_X$  is expected. The same argument helps explain why clusters at  $z = 1.09$  are slightly underluminous in the  $L_X$ - $\sigma_{\text{DM}}$  panel.

In summary, the scaling laws are in very good agreement with the evolution of the X-ray properties of simulated clusters. We discuss below how these results compare with previous work and with observations.

## 5. Comparison with previous work

### 5.1. Numerical simulations

Figure 15 compares the luminosity-temperature relation obtained from our simulations with that found in other numerical studies. At  $z = 0$ , this relation (open squares) compares well with that obtained by NFW95, Evrard (1990, labeled E90), and Bartelmann & Steinmetz (1996, labeled BS96) for  $\Omega_0 = 1$  CDM, once they are all scaled to the same gas mass fraction,  $f_{\text{gas}} = 0.1$ . This reflects the similarity of the structure of systems formed through hierarchical clustering (NFW96, NFW97). The curves labeled CO94, K94, and B94 correspond to the work of Cen & Ostriker (1994), Kang et al (1994), and Bryan et al (1994), respectively. K94 and B94 considered clusters in an  $\Omega_0 = 1$  CDM universe, while CO94 simulated clusters in an  $\Omega_0 = 0.45$ ,  $\Lambda_0 = 0.55$  CDM universe. The slope and normalization of the  $L_X$ - $T$  relation found by these authors are in disagreement with the results of this paper and of NFW95.

One simple explanation of this discrepancy is that the luminosities found by these other authors are severely compromised by numerical resolution. Indeed, the spatial resolution in the simulations of CO94, K94 and B94 (ie. the grid cell size in their Eulerian codes) is  $0.31h^{-1}$  Mpc, about three times larger than the core radii of our clusters (see Table 3). The core radii in the Eulerian simulations are thus largely set by the mesh size, and the corresponding X-ray luminosities are only lower bounds to the actual luminosity.

Several lines of argument support this conclusion: (i) The core radii in CO94, K94 and B94 are independent of cluster mass or temperature. This occurs because all clusters, regardless of mass or physical size, are analyzed in one single simulation with the same grid size, which fixes the core radii. In our work and in NFW95, the core radius is found to be proportional to the characteristic scale-length of the dark halo, and scales roughly as the virial radius of the system,  $r_{\text{core}} \propto r_{\text{vir}} \propto T^{1/2}$ . (ii) The slope of the  $L_X$ - $T$  relation in CO94, K94 and B94 is steeper than expected from the scaling laws. This is also easily explained if the gas core radii just reflect the spatial resolution of the calculation. Since cooler clusters are smaller in size, artificially fixed core radii affect cooler clusters more severely (ie. the core radius is a larger fraction of the virial radius), systematically depressing their X-ray luminosity. (iii) Finally, at a given temperature, the luminosities found by K94 and B94 differ by about a factor 2, even though they model clusters in exactly the same cosmogony using the same grid size, so at least one of them cannot be right. K94 and B94 use different numerical techniques, so the discrepancy is most likely due to the fact that in both cases the luminosity estimates are compromised by numerical resolution, but the *effective* spatial resolution is different in the two techniques.

Our interpretation is similar in spirit to that of Anninos & Norman (1996), who also argued that the X-ray luminosity of clusters in CO94, K94, and B94 had been severely underestimated. However, we disagree with Anninos & Norman’s conclusion that the X-ray luminosity of X-ray clusters does not converge as the numerical resolution is improved. NFW95 show that provided that adequate mass and spatial resolution are used, the X-ray luminosity is very robust to changes in the numerical parameters (see Figure 13 of NFW95 and the lower panel of Figure 11 above). Indeed, the key to the convergence of the X-ray luminosity lies in resolving the core radius of the gas which, according to Table 3, is  $r_{\text{core}} \approx 0.33r_s \approx 0.05r_{\text{vir}}$ . An effective spatial resolution better than 5% of the virial radius, and matching mass resolution (typically several thousand particles within  $r_{\text{vir}}$ ), are thus required for robust estimates of the X-ray luminosity. A very small fraction of the total luminosity comes from within the core because the gas density profile is shallower than  $r^{-1}$ , ensuring convergence of the total X-ray luminosity. A similar conclusion has been reached independently by Bryan & Norman (1997).



Further support for this conclusion comes from the test cluster comparison project mentioned in §1, in which the same cluster was simulated with different numerical techniques and varying resolution. Simulations that are able to resolve  $r_{\text{core}}$  give similar X-ray luminosities (Frenk et al. , in preparation). It is worth emphasizing that there is nothing intrinsically wrong with the numerical techniques used by CO94, K94 and B94. As the cluster comparison test demonstrates, SPH codes compare well with Eulerian codes and give essentially the same results in regions that are adequately resolved by both.

## 5.2. Observations

### 5.2.1. The $L_X$ - $T$ relation

Figure 16 compares the  $L_X$ - $T$  relation measured for nearby ( $z < 0.1$ , open circles) and distant ( $z > 0.2$ , filled circles) clusters with the scaling laws derived in §2 and calibrated as described in §4.6.3. All luminosities are bolometric and have been converted to  $q_0 = 0.5$ . Solid lines correspond to  $z = 0$ , and dashed lines to  $z = 0.3$  for two different cosmologies. The models have been normalized so that they agree at  $z = 0$ . The observed  $L_X$ - $T$  relation is steeper than predicted by the scaling laws. Although there is good agreement at the bright end, cool ( $T < 5$  keV) clusters are much fainter than expected.

This discrepancy was also noticed by NFW95, who argued that it was indicative of the role played by some non-gravitational mechanism, such as radiative cooling, consumption of gas into galaxies, or pre-heating, in establishing the X-ray properties of clusters. (See also Kaiser 1991, Evrard & Henry 1991, Bower 1997, for similar arguments.) For example, NFW95 showed that the observed  $L_X$ - $T$  relation can be reproduced if the gas in clusters were preheated to a common entropy before cluster assembly, a conclusion similar to that reached by Metzler & Evrard (1994). The good agreement between simulations and observations for hot ( $T > 5$  keV) is intriguing, and suggests that preheating is unimportant at these very high temperatures. This characteristic preheating entropy is an important clue that may allow us to constrain the mode and timing in which the preheating process operates (Ponman, Cannon & Navarro, in preparation).

At the modest redshifts probed by the data (clusters represented with filled circles span the redshift range  $\sim 0.2$ - $0.6$ , with a mean of  $\langle z \rangle \sim 0.3$ , see Mushotzky & Scharf 1997), there is little evidence for evolution in the slope or zero point of the  $L_X$ - $T$  relation (see also Henry, Jiao & Gioia 1994 and Tsuru et al. 1996). This, in fact, is in good agreement with the weak evolution expected from the scaling laws (eq.14). The short- and long-dashed lines in Figure 16 show the  $L_X$ - $T$  relation predicted by eq.(14) at  $z = 0.3$  for two different cosmogonies: a low-density and an Einstein-de Sitter CDM model, respectively. At a given temperature, clusters are expected to be no more than 30% more luminous at  $z \sim 0.3$  than at  $z = 0$ . Such a small difference would be very difficult to disentangle from the large scatter in the observed  $L_X$ - $T$  relation. We conclude that the evolution of the luminosity-temperature relation is consistent with that predicted by the scaling laws.

The scatter in the observed  $L_X$ - $T$  relation is about a factor of two to three larger than found in the simulations, although the large errors associated with many temperature measurements quoted in the literature make this a difficult point to assess. Provided errors are not the main source of the scatter, and since simulated clusters are at various stages of dynamical evolution, it appears that deviations from equilibrium cannot be solely responsible for the observed scatter. Further support for this assertion comes from the fact that deviations from the average  $L_X$ - $T$  relation correlate with the strength of the central cooling flow (Fabian et al 1994).

### 5.2.2. CNOC clusters

Figure 17 compares the dark matter projected density and line-of-sight velocity dispersion profiles, averaged over our ten simulated clusters (solid lines), with the corresponding profiles for *galaxies* in the clusters studied by the CNOC project (points with error bars, taken from Carlberg, Yee & Ellingson 1997). The CNOC data are based on  $\sim 2600$  redshifts collected in the fields of 16 X-ray luminous clusters at  $z \sim 0.3$ . All cluster profiles (observed and simulated) have been rescaled to their individual virial radius prior to averaging. The only free normalization is that of the dark matter density, which has been chosen to match the galaxy number density data.

The dark matter and galaxy profiles are remarkably similar. Thus, the structure of clusters in our low-density CDM model is consistent with the assumption that galaxies are, on average, fair tracers of the mass distribution in clusters. This is a useful result because one of the major uncertainties that plagues the analysis of dynamical data such as those collected by the CNOC group is the extent to which galaxies may be spatially segregated or dynamically ‘biased’ relative to the surrounding matter. These ‘biases’ are extremely difficult to detect and measure observationally. Neglecting them in a virial analysis of the CNOC data leads to an estimate of  $\Omega_0 = 0.24 \pm 0.14$  (Carlberg et al. 1996), consistent with our assumed value of  $\Omega_0 = 0.3$ . Thus, our results suggest that there is little segregation between mass and galaxies in X-ray luminous clusters, as concluded independently by the CNOC team (Carlberg et al. 1996). It is unclear, however, whether this conclusion is compatible with the large-scale clustering properties of a flat,  $\Omega_0 = 0.3$  CDM universe which require galaxies to be significantly antibiased relative to the mass on cluster scales (Jenkins et al. 1997).

## 6. Conclusions

We have used N-body/gasdynamical simulations to study the structure and evolution of X-ray clusters formed in a low-density CDM universe ( $\Omega_0 = 0.3$ ,  $\Lambda_0 = 0.7$ ,  $h = 0.7$ ,  $\sigma_8 = 1.05$ ). The simulations include gravity, pressure gradients and hydrodynamical shocks, but neglect the effects of radiative cooling or of galaxy formation. A summary of our main conclusions follows.

- (1) The density profiles of clusters of different mass identified at various redshifts are described accurately by the fitting formula proposed by Navarro, Frenk & White (eq. 3; see also NFW95 and NFW96). The parameters of the fit are in good agreement with the analytical model proposed by these authors (NFW97). This formula provides an adequate description of the mass profile over approximately two decades in radius, out to the ‘virial’ radius beyond which infall dominates. The extent of this virialized region is consistent with a definition of ‘virial radius’ based on the spherical top-hat collapse model.
- (2) The structure of cluster dark matter halos is in excellent agreement with the distribution and dynamics of galaxies in the clusters analyzed by the CNOC project. This is consistent with the idea that galaxies and dark matter in clusters are not spatially segregated or dynamically biased to a significant degree.
- (3) The gas density profiles of simulated clusters differ significantly from the dark matter profiles and are better described using the  $\beta$ -model (eq.17). However, the gas and dark matter density profiles remain proportional to each other regardless of cluster mass and redshift. Numerical estimates of the X-ray luminosity converge quickly when the scale radius of the dark matter and the core radius of the gas are resolved numerically. For an SPH simulation, this typically requires  $\gtrsim 3 \times 10^3$  particles per cluster and an effective spatial resolution better than about one percent of the virial radius.

(4) The structural similarity between the dark and gas components implies that simple scaling laws relate the mass, velocity dispersion, temperature, and X-ray luminosity of galaxy clusters. These scaling laws can be derived using the fact that clusters of a given mass are described by a single free parameter: their characteristic density or concentration. These laws extend the scale-free relations of Kaiser (1986) to universes with  $\Omega \neq 1$  and perturbation spectra different from power-laws. The predictions of these scaling laws, as a function of cluster mass and redshift, are in remarkable agreement with the results of the simulations. This provides an impressive validation of the Smooth Particle Hydrodynamics technique.

(5) The X-ray luminosity in simulated clusters scales approximately as the square of the temperature, roughly as predicted by the scaling laws. This is a shallower dependence of  $L_X$  on  $T$  than is observed for X-ray clusters. We interpret this disagreement as requiring additional physical processes not included in these simulations (eg. radiative cooling or preheating) to account for the X-ray properties of clusters, particularly of low-temperature ( $kT < 5$  keV) systems. This relation is expected to evolve only weakly with redshift. At a given temperature clusters are not expected to brighten by more than 30% at  $z \sim 0.3$ , consistent with published measurements.

(6) The average baryon fraction within the virial radius is 85-90% of the universal mean,  $\Omega_b/\Omega_0$ , and is lower in the inner regions. This result calls for caution when interpreting the baryon fraction measured in clusters in terms of the universal mean. The inclusion of physical processes neglected here, such as radiative cooling, may affect the cluster baryon fraction although such effects are likely to be small.

(7) X-ray emission-weighted temperatures can be used to estimate reliably the total mass and velocity dispersion of clusters (eqs. 18 and 19). These estimators are essentially unbiased and have small scatter,  $\sim 20\%$  for the mass-temperature, and  $\sim 15\%$  for the mass-velocity relations. A consequence of this is that semianalytical techniques and N-body simulations can be used to predict the statistical properties of X-ray clusters in different cosmological models without the need for expensive hydrodynamical simulations.

Physical processes not included in our simulations, such as radiative cooling, galaxy formation, or non-gravitational heating may all have a significant effect on the temperature of the intracluster medium and on the X-ray luminosity of galaxy clusters. We have chosen to neglect them in this study, and to concentrate instead on the simpler ‘adiabatic’ evolution of gas within an evolving population of dark matter halos. The failure of ‘adiabatic’ clusters to reproduce the observed luminosity-temperature relation indicates that additional physics must be included in the numerical modeling in order to develop a full understanding of the origin and evolution of the X-ray properties of galaxy clusters. We are currently working on these issues.

## Acknowledgments

We thank Douglas Heggie for supporting the GRAPE hardware in Edinburgh. Hugh Couchman kindly made available his excellent AP<sup>3</sup>M code, and Ray Carlberg provided the CNOC data used in Figure 17. JFN acknowledges useful discussions with Matthias Steinmetz. VRE acknowledges the support of a PPARC studentship and a PPARC Postdoctoral Fellowship, and CSF a PPARC Senior Research Fellowship. This research has been supported by the UK PPARC.

Table 1: Parameters of resimulated clusters. (1) The label for each run; (2) the comoving size of the ‘high-resolution’ box; (3) the number of gas particles in the high-resolution region (an equal number of dark matter particles was used in each run); (4) the mass of each gas particle (dark matter particles are nine times heavier); and (5) the ‘formation’ redshift, ie. the redshift at which the mass of the most massive progenitor first exceeds half the final mass of the system.

(1) Label	(2) $l_{\text{hr}}$ $h^{-1}\text{Mpc}$	(3) $N_{\text{gas}}^{\text{tot}}$	(4) $m_{\text{gas}}$ $10^9 h^{-1} \text{M}_{\odot}$	(5) $z_{1/2}$
cl01a	42.2	42875	14.6	0.71
cl02a	42.2	64000	9.77	0.35
cl03a	39.4	54872	9.26	0.87
cl04a	33.8	39304	8.14	0.18
cl05a	36.6	54872	7.42	0.18
cl06a	39.4	64000	7.94	0.89
cl07a	42.2	64000	9.77	0.53
cl08a	42.2	64000	9.77	0.18
cl09a	36.6	64000	6.36	0.32
cl10a	33.8	50653	6.32	0.68
average	$\langle 38.3 \rangle$	$\langle 56258 \rangle$	$\langle 8.93 \rangle$	$\langle 0.47 \rangle$

Table 2: Bulk properties of clusters identified at  $z = 0$ . (1) The run label; (2) the virial mass; (3) the virial radius, (4) the 1D dark matter velocity dispersion, defined as  $(2K_{\text{DM}}/3)^{1/2}$ , where  $K_{\text{DM}}$  is the specific kinetic energy ; (5) the X-ray emission-weighted gas temperature; (6) the X-ray luminosity; (7) the ratio between the gas kinetic and thermal energies; (8) the radius that contains half of the total X-ray luminosity; (9) the gas mass fraction; (10) the number of gas particles; and (11) the number of dark matter particles. All quantities are computed using particles within the virial radius of each system.

(1)	(2)	(3)	(4)	(5)	(6)	(7)	(8)	(9)	(10)	(11)
Label	$M_{\text{vir}}$ $10^{14} h^{-1} \text{M}_{\odot}$	$r_{\text{vir}}$ $h^{-1} \text{Mpc}$	$\sigma_{\text{DM}}$ $\text{kms}^{-1}$	$kT_{\text{gas}}$ keV	$L_X$ $h^{-2} \text{ ergs}^{-1}$	KE/U	$r_{\text{L}/2}$ $[r_{\text{vir}}]$	$f_{\text{gas}}$	$N_{\text{gas}}$	$N_{\text{DM}}$
cl01a	16.0	2.42	1139	9.9	8.01e44	0.14	0.084	0.086	9387	11146
cl02a	15.4	2.39	1075	8.5	7.96e44	0.30	0.066	0.086	13634	16008
cl03a	14.8	2.36	1077	7.8	6.59e44	0.14	0.080	0.087	13876	16242
cl04a	9.65	2.04	952	5.0	3.55e44	0.60	0.089	0.090	10688	11977
cl05a	9.59	2.04	1153	9.7	1.08e45	0.51	0.093	0.091	11760	13065
cl06a	10.1	2.08	942	6.9	4.98e44	0.12	0.072	0.086	11015	12937
cl07a	8.45	1.96	926	5.9	2.43e44	0.21	0.103	0.085	7367	8798
cl08a	8.16	1.93	960	6.9	2.36e44	0.60	0.111	0.086	7176	8484
cl09a	6.32	1.78	775	3.1	4.80e43	0.57	0.481	0.081	8087	10149
cl10a	7.84	1.91	952	6.2	3.18e44	0.22	0.100	0.092	11414	12513
average	$\langle 10.63 \rangle$	$\langle 2.09 \rangle$	$\langle 995 \rangle$	$\langle 7.0 \rangle$	$\langle 5.03 \rangle$	$\langle 0.34 \rangle$	$\langle 0.128 \rangle$	$\langle 0.087 \rangle$	$\langle 10440 \rangle$	$\langle 12132 \rangle$

Table 3: Parameters of density profile fits. Dark matter profiles are fitted using eq.(3) and gas profiles using eq.(17). Each column lists the following parameter: (1) The run label; (2) the redshift at which the fit is done; (3) the virial radius; (4) the dark matter characteristic density, expressed in units of the current critical density; (5) the dark matter scale radius; (6) the gas central density, in units of the current critical density; (7) the gas core radius; and (8) the outer slope parameter  $\beta_{\text{fit}}$  (see eq.17). The rows labeled ‘average’ correspond to fits to the average profile of the ten most massive progenitors of each cluster at each redshift (see Figure 10).

(1) Label	(2) Redshift	(3) $r_{\text{vir}}$ $h^{-1}\text{Mpc}$	(4) $\delta_c$ $[\rho_{\text{crit}}]$	(5) $r_s$ $h^{-1}\text{Mpc}$	(6) $\delta_0$ $[\rho_{\text{crit}}]$	(7) $r_{\text{core}}$ $h^{-1}\text{Mpc}$	(8) $\beta_{\text{fit}}$
cl01a	0.00	2.42	9.69e3	0.320	1.74e3	0.159	0.828
cl02a	0.00	2.39	7.13e3	0.349	2.89e3	0.108	0.776
cl03a	0.00	2.36	5.58e3	0.397	1.90e3	0.139	0.797
cl04a	0.00	2.04	5.81e3	0.314	1.90e3	0.106	0.779
cl05a	0.00	2.04	1.12e4	0.268	1.80e3	0.169	0.931
cl06a	0.00	2.08	1.05e4	0.261	2.45e3	0.105	0.768
cl07a	0.00	1.96	4.86e3	0.363	1.12e3	0.146	0.783
cl08a	0.00	1.93	5.46e3	0.337	7.70e2	0.199	0.865
cl09a	0.00	1.78	2.22e3	0.405	3.48e2	0.047	0.366
cl10a	0.00	1.91	8.17e3	0.283	1.14e3	0.173	0.865
average	0.00	2.09	6.91e3	0.323	1.97e3	0.105	0.735
average	0.38	1.35	6.23e3	0.240	1.62e3	0.081	0.712
average	1.09	0.69	3.32e3	0.187	1.11e3	0.061	0.749

Table 4: Table of mean  $\beta$  parameters for clusters identified at different redshifts. Errors are standard deviations of the sample of ten clusters.

Redshift	$\bar{\beta}_{TM}$	$\bar{\beta}_{T\sigma}$
0	$0.98 \pm 0.07$	$0.90 \pm 0.04$
0.55	$1.10 \pm 0.04$	$0.99 \pm 0.04$
1.09	$1.12 \pm 0.07$	$0.97 \pm 0.03$

## REFERENCES

- Anninos P., Norman M. L., 1996, ApJ, 459, 12
- Bartelmann, M., & Steinmetz, M., 1996, MNRAS 283, 431.
- Bond, J.R. & Efstathiou, G., 1984, ApJL 285, L45.
- Bower, R.G., 1997, MNRAS 288, 355.
- Bryan G. L., & Norman M. L., 1997, in “Computational Astrophysics”, Proceedings of the 12th Kingston Conference, PASP Conference Series, eds. D.Clarke & M.West (astro-ph/9710186).
- Bryan G. L., Cen R., Norman M. L., Ostriker J. P., Stone J. M., 1994, ApJ, 428, 405
- Carlberg R. G., Yee H. K. C., Ellingson E., Abraham R., Gravel P., Morris S., Pritchet C. J., 1996, ApJ, 462, 32
- Carlberg R. G., Yee H. K. C., Ellingson E., 1997, ApJ, 478, 462
- Cavaliere, A. and Fusco-Femiano, 1976, Astron. Astrophys., 49, 137.
- Cen R., Ostriker J. P., 1994, ApJ, 429, 4
- Cole S., Lacey C., 1996, MNRAS, 281, 716
- Copi C. J., Schramm D. N., Turner M. S., 1995, Science, 267, 192
- Couchman H. M. P., 1995, in Numerical Methods in Astrophysics, Vol. II, Springer-Verlag, New York, in press
- Couchman H. M. P., Thomas P. A., Pearce F. R., 1995, ApJ, 452, 797
- Crone M. M., Evrard A. E., Richstone D. O., 1994, ApJ, 434, 402
- David L. P., Jones C., Forman W., 1995, ApJ, 445, 578
- Edge A. C., Stewart G. C., Fabian A. C., Arnaud K. A., 1990, MNRAS, 245, 559
- Eke V. R., Cole S., Frenk C. S., 1996, MNRAS, 282, 263
- Evrard A. E., 1990a, in *Clusters of Galaxies*, eds. M. Fitchett and W. Oegerle (Cambridge: Cambridge University Press), p.287
- Evrard A. E., 1990b, ApJ, 363, 349
- Evrard A. E., 1997, MNRAS, submitted (astro-ph/9701148)
- Evrard A. E., Henry J. P., 1991, ApJ, 383, 95
- Evrard A. E., Metzler C. A., Navarro J. F., 1996, ApJ, 469, 494
- Fabian, A.C., Crawford, C.S., Edge, A.C., & Mushotzky, R.F., 1994, MNRAS 267, 779.
- Gioia I. M., Henry J. P., Maccacaro T., Morris S. L., Stocke J. T., Wolter A., 1990, ApJ, 356, L35



- Gunn K. F., Thomas P. A., 1996, MNRAS, 281, 1133
- Henry J. P., 1997, ApJL, 489, L1.
- Henry J. P., Jiao L., Gioia I. M., 1994, ApJ, 432, 49
- Jenkins A. R., et al. , 1997, in “Dark and Visible Matter in Galaxies”, PASP Conference Series, vol.117, eds. Persic, M. and Salucci, P., p.348. (astro-ph/9610206)
- Jones, C. and Forman, W. 1984, ApJ, 276, 38.
- Kaiser N., 1986, MNRAS, 222, 323
- Kaiser N., 1991, ApJ, 383, 104
- Kang H., Cen R., Ostriker J. P., Ryu D., 1994, ApJ, 428, 1
- Lacey C., Cole S., 1993, 262, 627
- Lacey C., Cole S., 1994, 271, 676
- Loewenstein M., Mushotzky R. F., 1996, ApJ, 471, L83
- Markevitch M., Mushotzky R. , Inoue H., Yamashita K., Furuzawa A., Tawara Y., 1996, ApJ, 456, 437
- Metzler C. M., Evrard A. E., 1994, ApJ, 437, 564
- Mohr J. J., Evrard A. E., Fabricant D.G., Geller M. J., 1995, ApJ, 447, 8
- Mushotzky R. F., Scharf C. A., 1997, ApJ, 482, L13
- Navarro J. F., White S. D. M., 1993, MNRAS, 265, 271
- Navarro J. F., Frenk C. S., White S. D. M., 1995, MNRAS, 275, 720 (NFW95)
- Navarro J. F., Frenk C. S., White S. D. M., 1996, ApJ, 462, 563 (NFW96)
- Navarro J. F., Frenk C. S., White S. D. M., 1997, ApJ, 490, 493 (NFW97).
- Nichol R. C., Holden B. P., Romer A. K., Ulmer M. P., Burke D. J., Collins C. A., 1997, ApJ, 481, 644
- Owen J. M., Villumsen J. V., 1997, ApJ, 481, 1
- Pearce F., Thomas P. A., Couchman H. M. P., 1994, MNRAS, 268, 953
- Rosati, P., Della Ceca, R., Norman, C., & Giacconi, R., 1998, ApJL, 492, L21.
- Rugers M., Hogan C. J., 1996, AJ, 111, 2135
- Smoot G. F., et al., 1992, ApJ, 396, L1
- Songaila A., Wampler E. J., Cowie L. L., 1997, Nat, 385, 137
- Steigmann G. Tosi M., 1995, ApJ, 453, 173
- Steinmetz M., 1996, MNRAS, 278, 1005

- Thomas P. A., Couchman H. M. P., 1992, MNRAS, 257, 11
- Tsuru T., Koyama K., Hughes J. P., Arimoto N., Kii T., Hattori M., 1996, eds Watanabe T., Yamashita K.,  
“The 11th international colloquium on UV and X-ray spectroscopy of Astrophysical and Laboratory  
Plasmas”, in press
- Tytler D., Fan X.-M., Burles S., 1996, Nat, 381, 207
- Viana P.T.P., Liddle A.R., 1996, MNRAS281, 323
- Walker T. P., Steigman G., Schramm D. M., Olive K. A., Kang H.-S., 1991, ApJ, 376, 51
- White D. A., Fabian A. C., 1995, MNRAS, 273, 72
- White S. D. M., 1982, in Saas-Fee Lectures “Morphology and Dynamics of Galaxies”, eds. L.Martinet and  
M.Mayor, (Geneva Observatory: Geneva), p.290
- White S. D. M., Rees M. J., 1978, MNRAS, 183, 341
- White S. D. M., Efstathiou G., Frenk C. S., 1993, MNRAS, 262, 1023
- White S. D. M., Navarro J. F., Evrard A. E., Frenk C. S., 1993, Nat, 366, 429

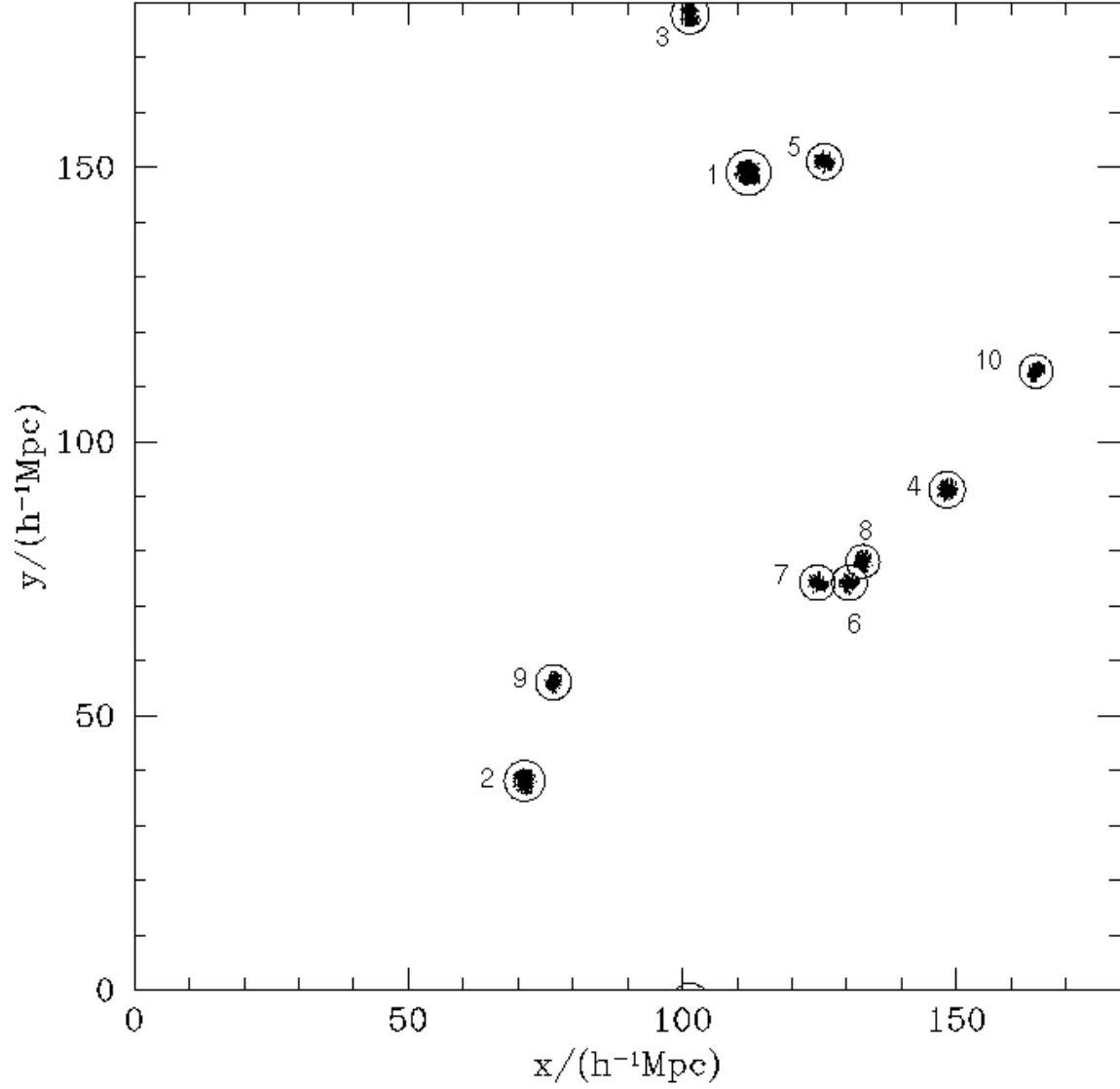


Fig. 1.— The projected positions of the ten most massive clusters in the original AP<sup>3</sup>M simulation. Each dot represents one dark matter particle associated with a cluster. The circles around each system have radii 1.5 times the virial radius. Clusters 6, 7 and 8 are physically close to each other. The closest separation between clusters is everywhere greater than  $9 h^{-1}\text{Mpc}$ .

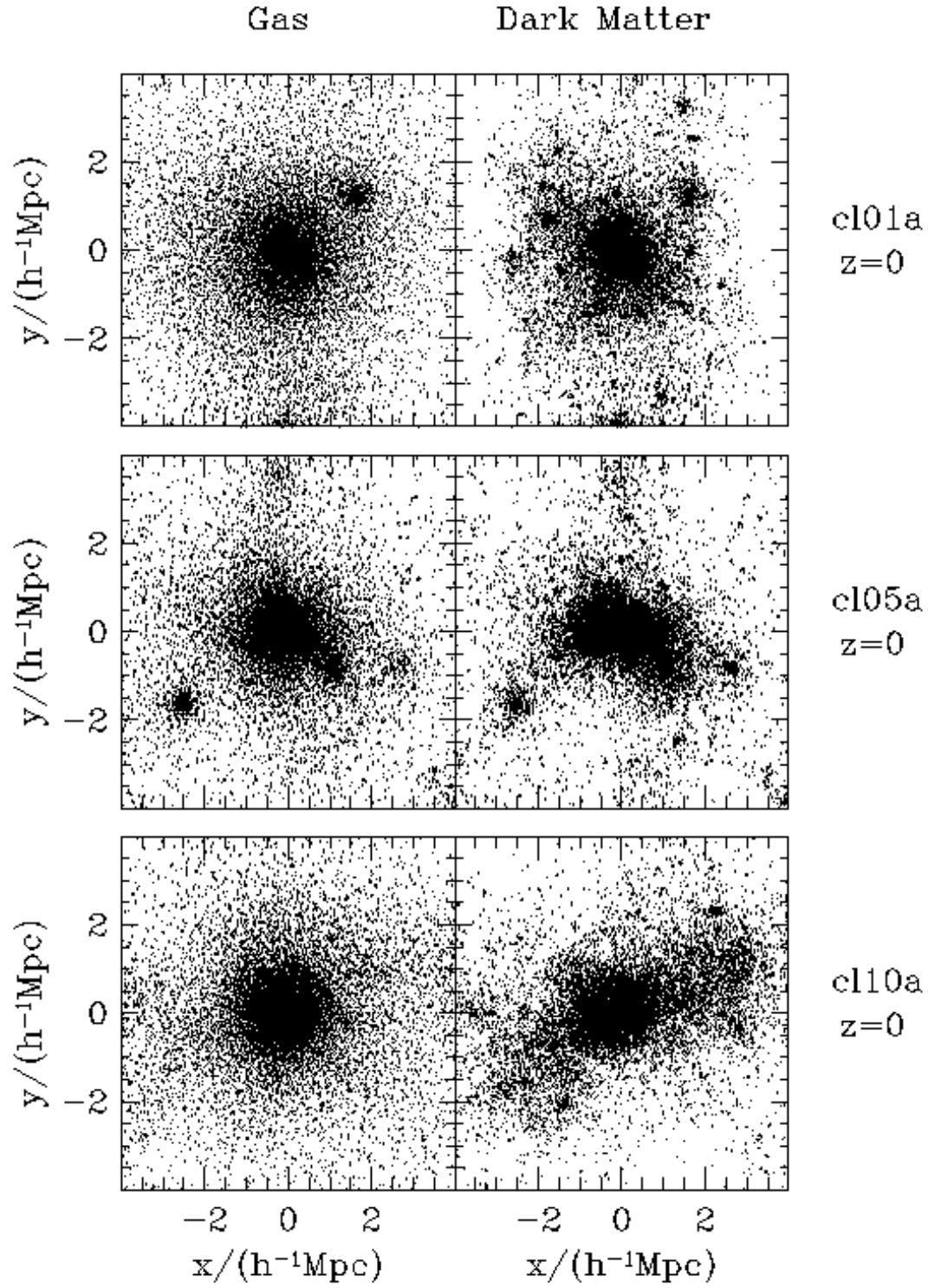


Fig. 2.— Dot plots showing projected particle positions at  $z = 0$  in cubes of side  $8 h^{-1}\text{Mpc}$  centred on three of the resimulated clusters.

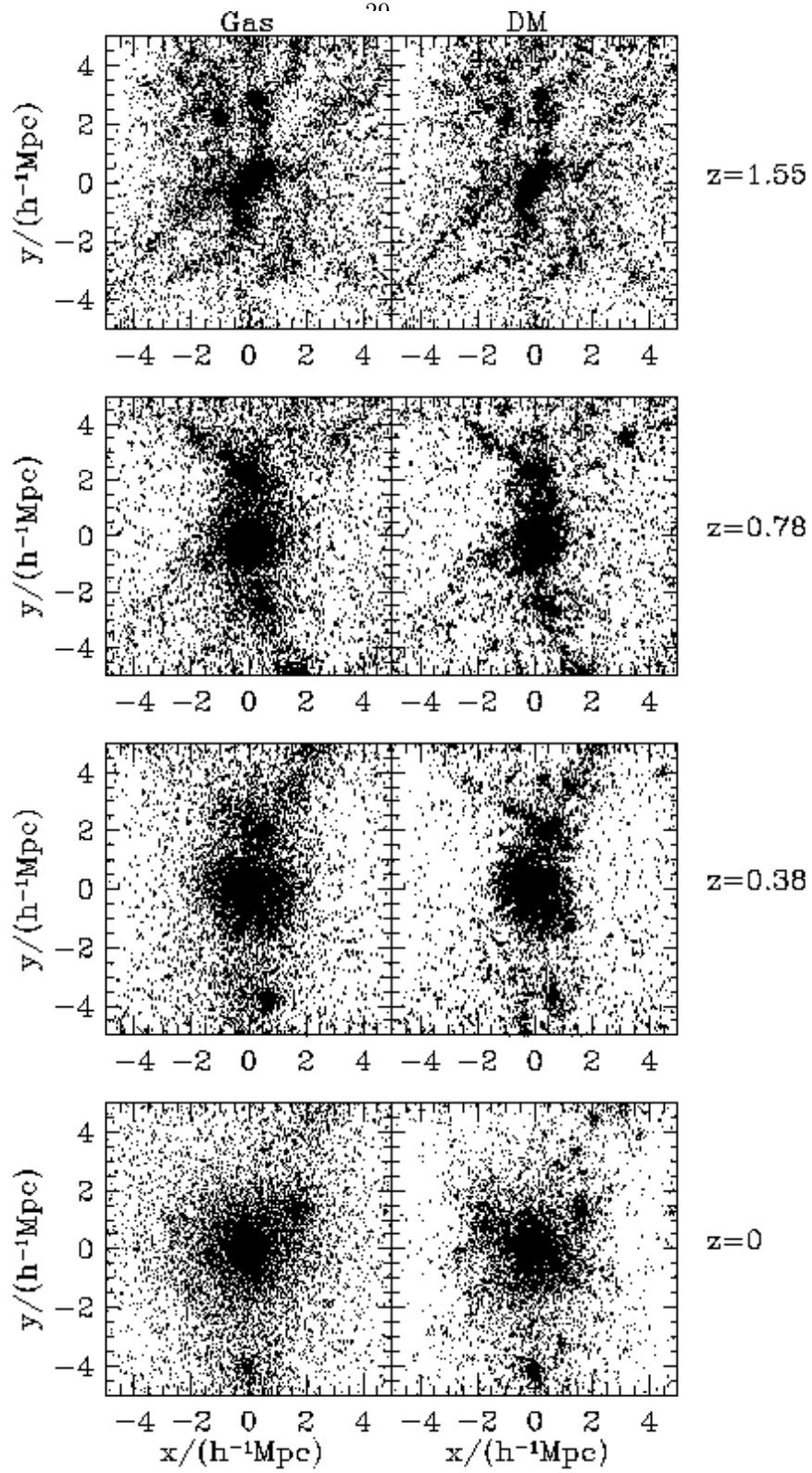


Fig. 3.— Dot plots showing the projected particle positions in cubes of physical size  $10 h^{-1} \text{Mpc}$  centred on cluster cl01a at different times. For clarity we plot only a random sample of half the particles in each panel.

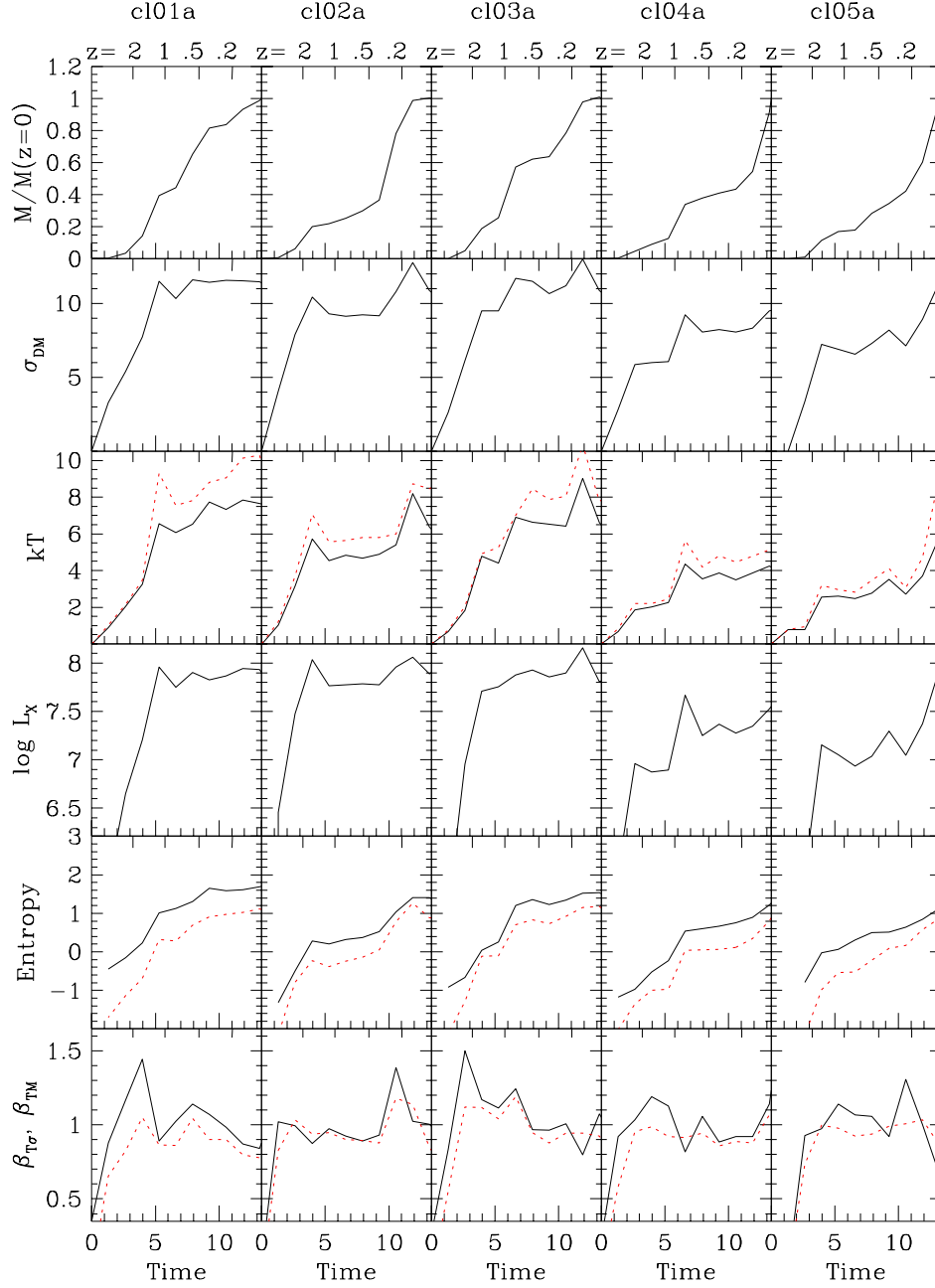


Fig. 4.— The evolution of bulk properties of clusters cl01a-cl05a. All properties refer to, and are computed within, the current virial radius of the most massive progenitor of each system. Each row contains the following information: (1) virial mass, normalized to the mass at  $z = 0$ ; (2) dark matter velocity dispersion (in units of  $100 \text{ km s}^{-1}$ ); (3) mass- and X-ray emission-weighted temperature in keV (solid and dotted lines, respectively); (4) bolometric X-ray luminosity, in units of  $10^{37} h^{-2} \text{ erg s}^{-1}$ ; (5) average ‘central entropy’ of the innermost 10% of the gas (dotted line) and dark matter (solid line) in the units given in §3.4.2; (6) ‘beta’-parameters:  $\beta_{TM}$  (solid line) and  $\beta_{T\sigma}$  (dotted line), defined in eqs. (18) and (19)

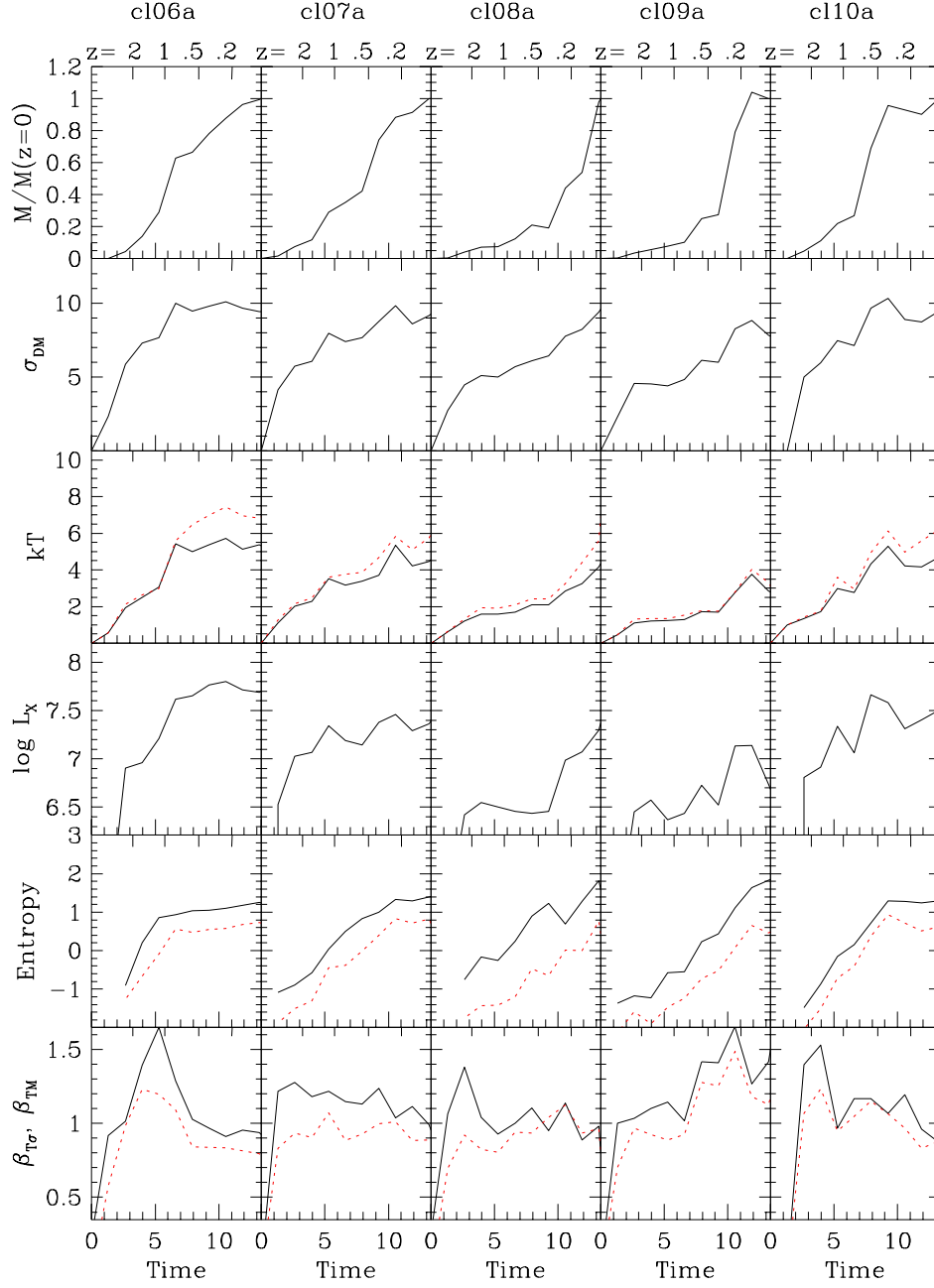


Fig. 5.— As Figure 4 for clusters cl06a-cl10a.

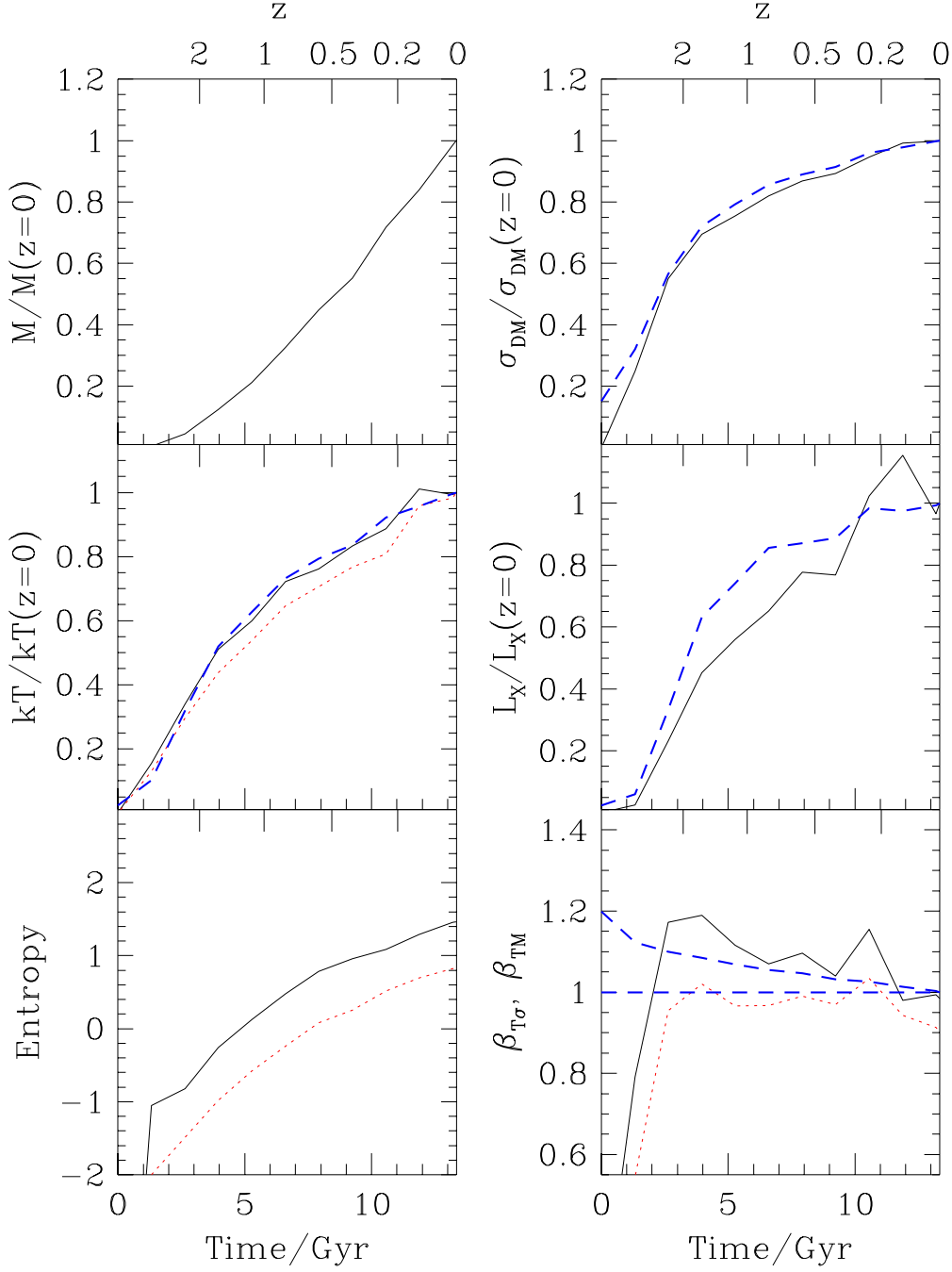


Fig. 6.— Evolution of bulk cluster properties averaged over all ten clusters. Quantities and line types are the same as those in Figures 4 and 5. Mass, velocity dispersion, temperatures, and luminosity are shown as a fraction of the final value. The thick dashed lines correspond to the evolution in each quantity derived from the scaling laws derived in §2 for a cluster with mass equal to that in the upper left panel. The two thick dashed lines in the lower right panel correspond to the scaling laws for  $\beta_{T\sigma} = 1$  (eqs. 12 and 18) and  $\beta_{TM} \propto H(c)^{-1}$  (eqs. 11 and 20).



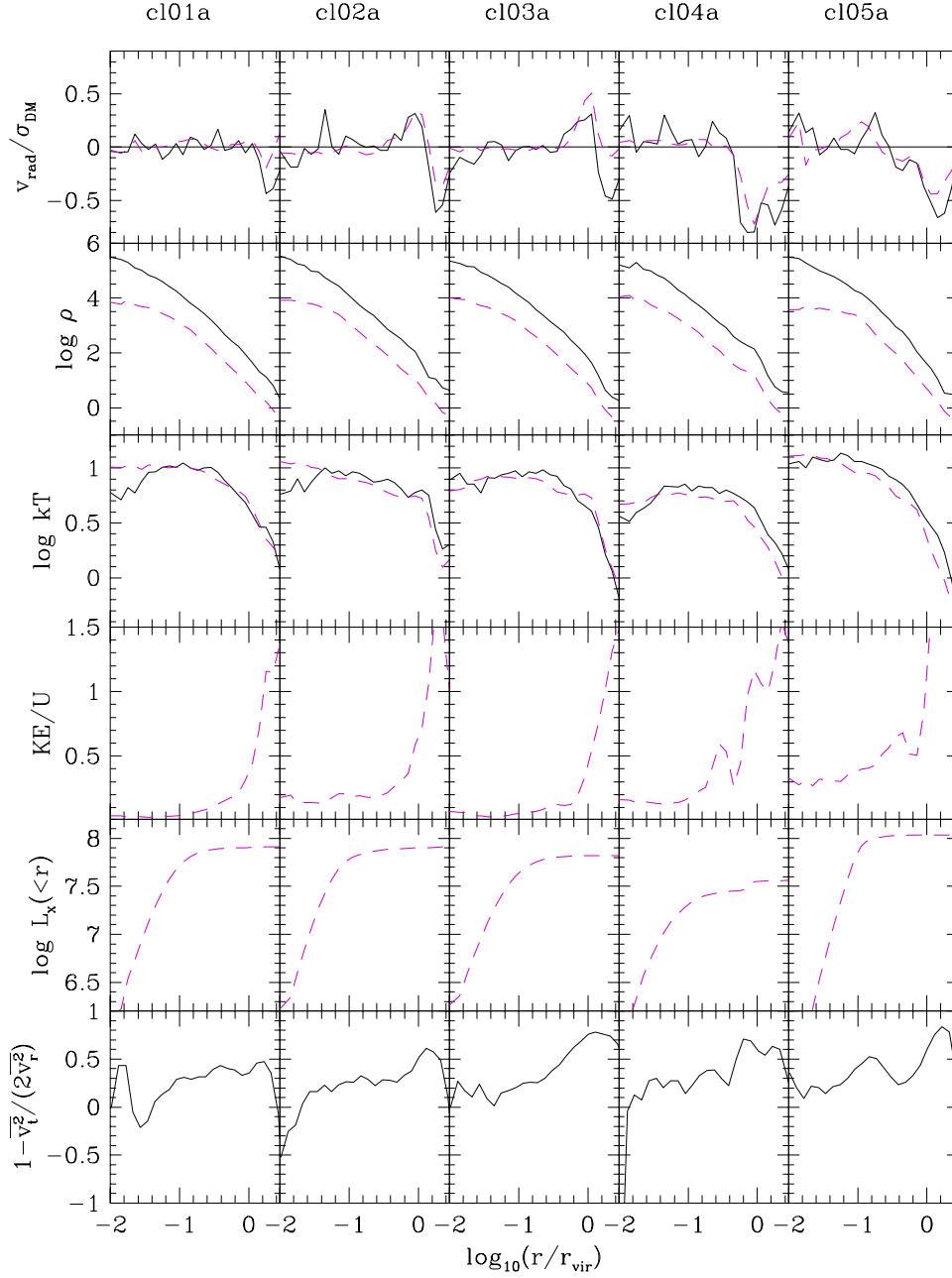


Fig. 7.— Spherically averaged profiles for clusters cl01a-cl05a at  $z = 0$ . Solid lines refer to the dark matter and dashed lines to the gas, respectively. Each row, from top to bottom, shows the following: (1) mean radial velocity in units of the dark matter velocity dispersion; (2)  $\log_{10}$  of the density expressed in units of the mean background value; (3)  $\log_{10}$  of the gas temperature in keV (dashed line) and  $\log_{10}$  of the dark matter ‘temperature’ (solid line), defined as  $\mu m_p \sigma_{\text{DM}}^2$ , where the velocity dispersions in each shell are relative to the radial mean (see first row); (4) ratio between gas kinetic and internal energies in each radial shell; (5)  $\log_{10}$  of the cumulative X-ray luminosity in units of  $10^{37} h^{-2} \text{ erg s}^{-1}$ ; and (6) dark matter velocity anisotropy,  $\beta_{\text{an}}$ .

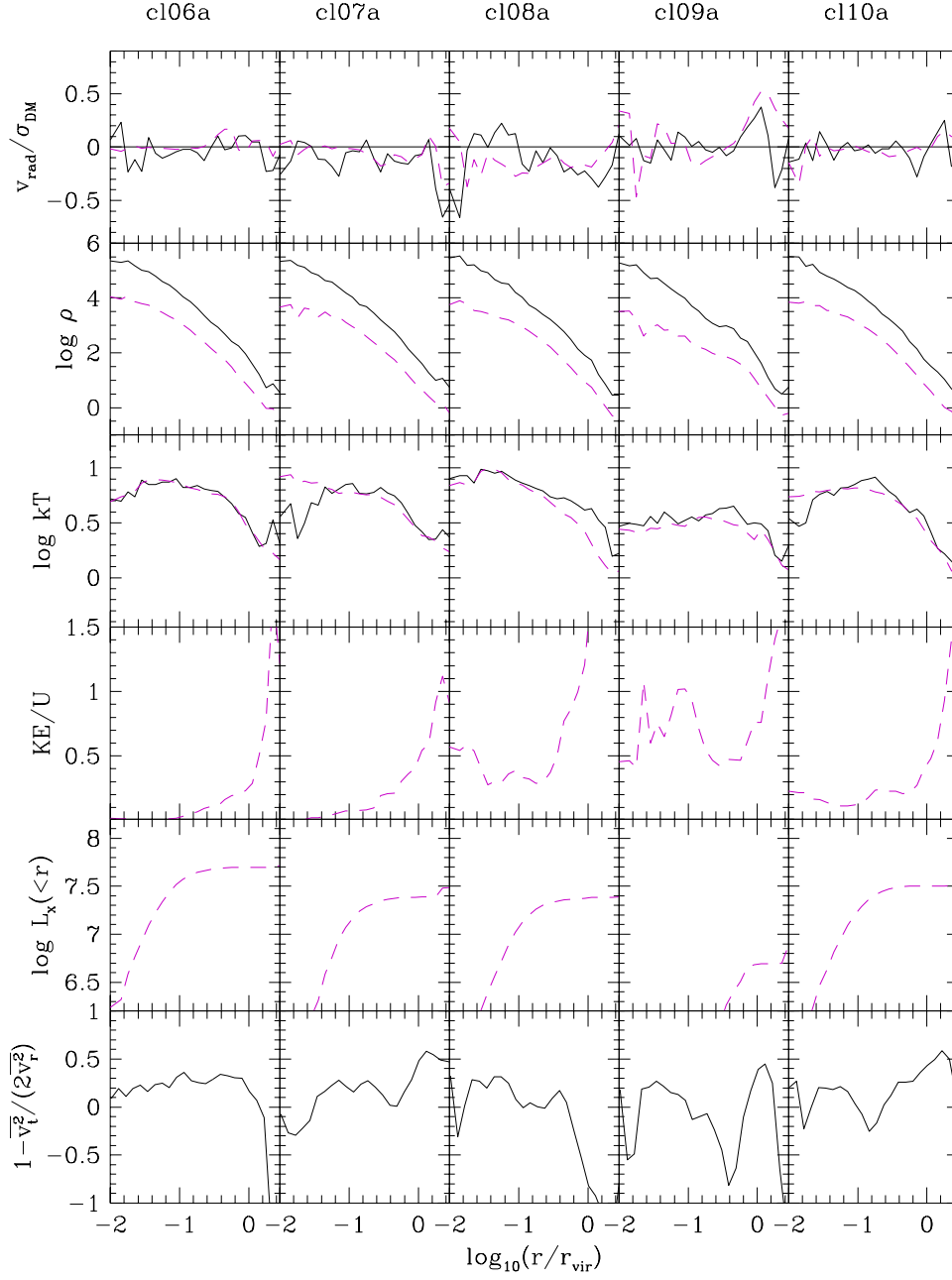


Fig. 8.— As Figure 7, but for clusters cl06a-cl10a.

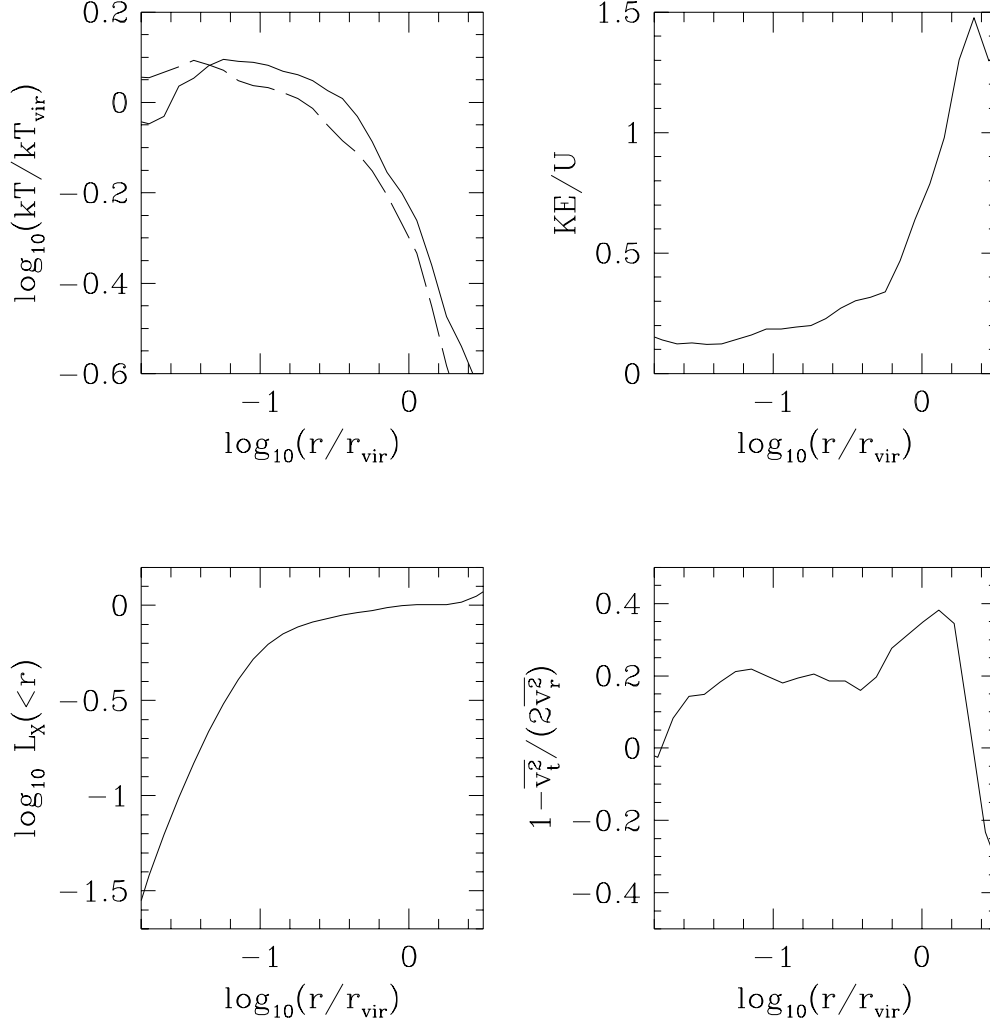


Fig. 9.— Radial profiles averaged over the ten clusters at  $z = 0$ . Upper left: gas and dark matter temperature profiles (dashed and solid lines, respectively). Temperatures are expressed in units of the virial temperature defined in eq.(16). See caption to Figures 7 and 8 for details. Upper right: ratio of bulk kinetic to thermal energies of the gas. Lower left: cumulative X-ray luminosity, normalized to the total luminosity of each cluster within the virial radius. Lower right: velocity anisotropy profile for the dark matter.

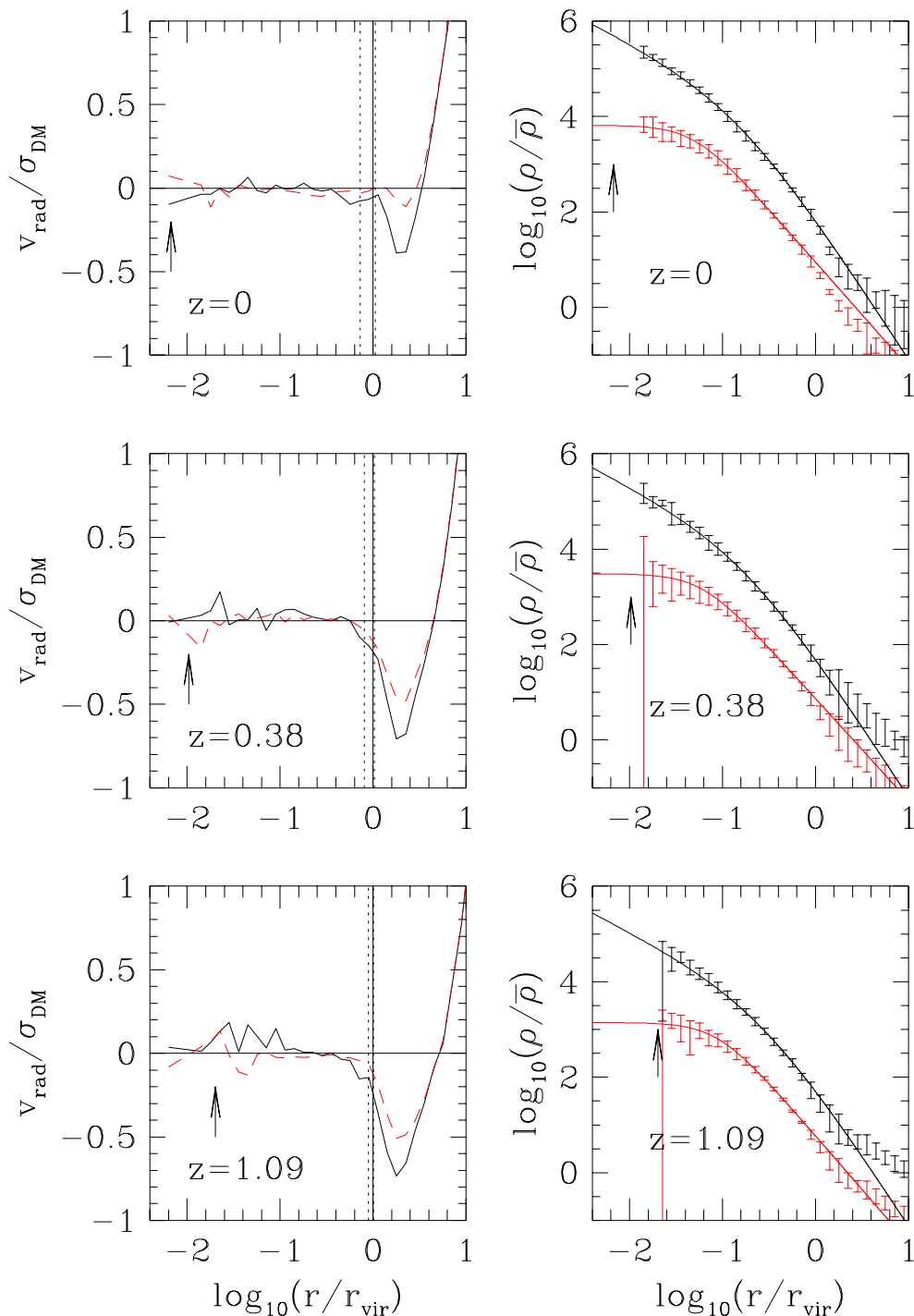


Fig. 10.— (1) Left panels: spherically averaged velocity profiles of gas (dashed lines) and dark matter (solid lines), averaged over all ten clusters at three different redshifts (see labels). Vertical lines correspond to  $r_{\text{vir}}$  (solid line), to  $r_{200}$ , the radius enclosing a mean inner density of 200 times the critical value (dotted line at  $r < r_{\text{vir}}$ ), and to the radius at which the time to complete a circular orbit equals the current age of the universe (dotted line at  $r \geq r_{\text{vir}}$ ). (2) Right panels: density profiles of gas and dark matter, averaged over all ten clusters. Best fits to the dark matter profiles using eq. (3) are shown. A  $\beta$ -model is used, instead, to fit the gas profiles. The parameters of these fits are given in Table 3. Error bars represent the standard deviation in the mean overdensity at each radius. In each panel the average softening scale is illustrated by an arrow.

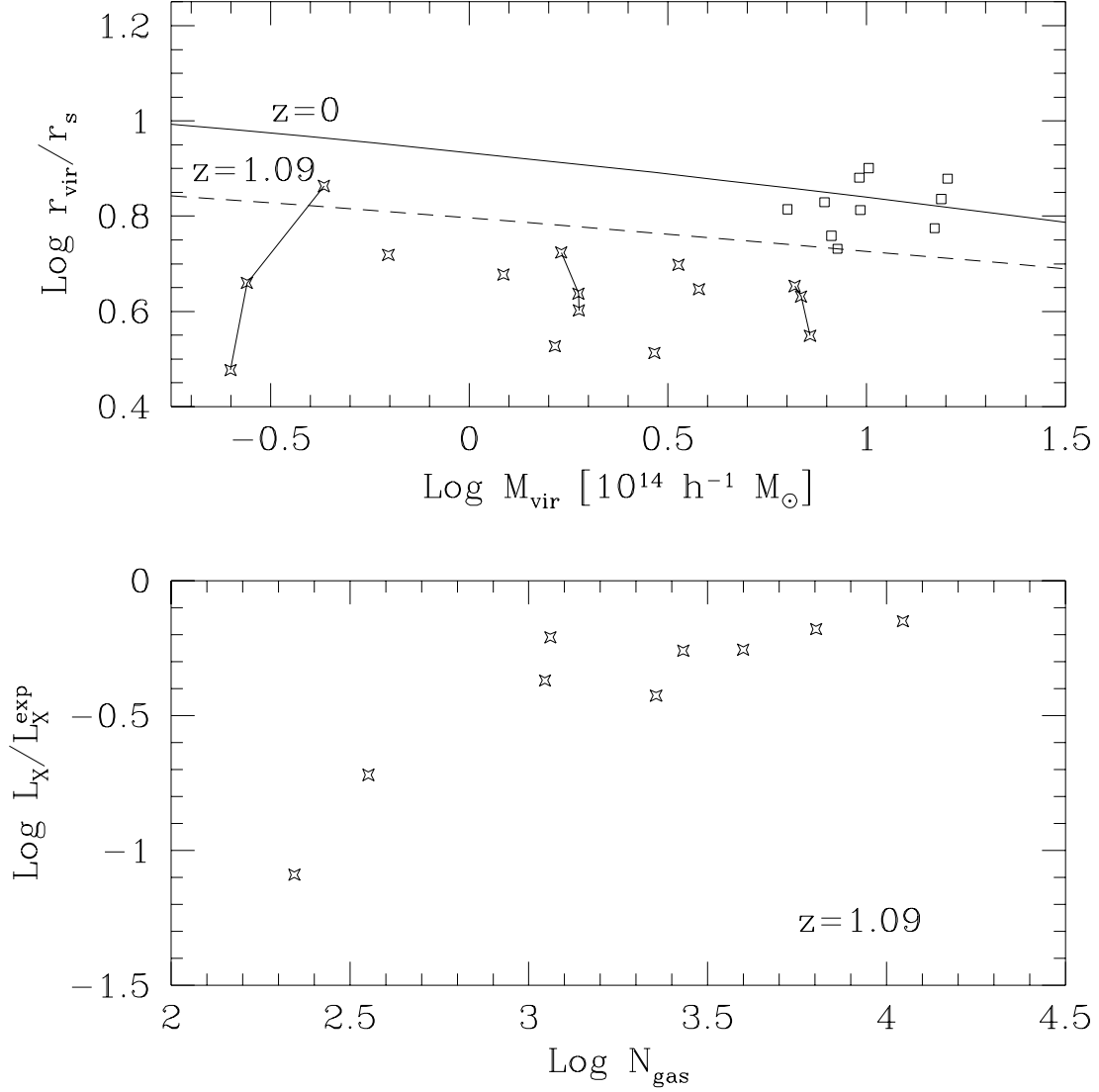


Fig. 11.— Top panel: best-fitting dark matter “concentrations” of simulated clusters versus virial mass. The two lines correspond to the concentrations expected for clusters at  $z = 0$  (solid) and  $z = 1.09$  (dashed) as given by the algorithm of NFW97. Squares and starred symbols correspond to simulated clusters at  $z = 0$  and 1.09, respectively. Symbols connected by lines correspond to the same cluster, simulated with three different particle numbers. See text for details. Bottom panel: X-ray luminosity estimates for the three clusters simulated with different particle numbers, as a function of the number of gas particles inside the virial radius. Each was evolved three times, increasing the number of particles successively by factors of two. The X-ray luminosity is normalized to the luminosity expected according to the scaling laws described in §2 (see dashed line in upper-left panel of Figure 13).

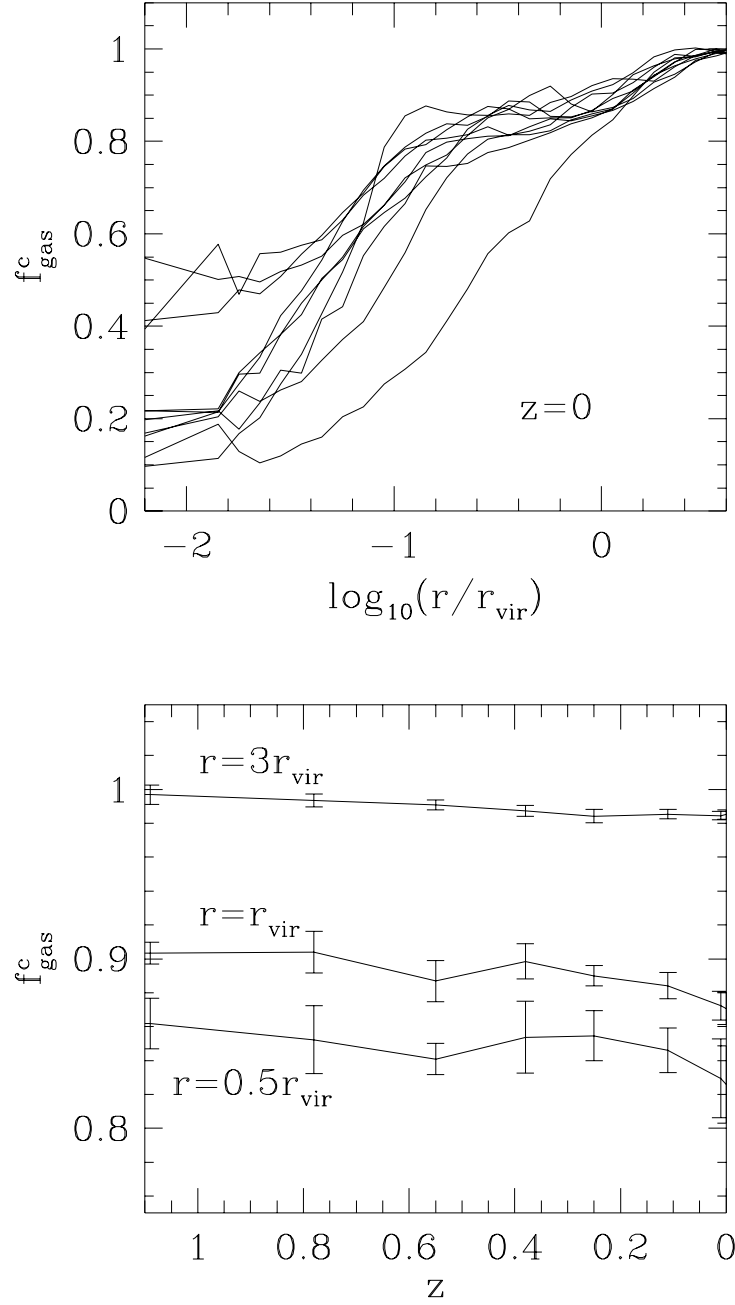


Fig. 12.— Top panel: cumulative gas fraction for all ten clusters at  $z = 0$ , expressed in units of the universal mean assumed in the numerical simulations,  $\Omega_b/\Omega_0 = 0.1$ . Bottom panel: gas fractions within three different radii, averaged over the ten most massive progenitors identified at different redshifts. Error bars give the standard deviation in a single cluster measurement.

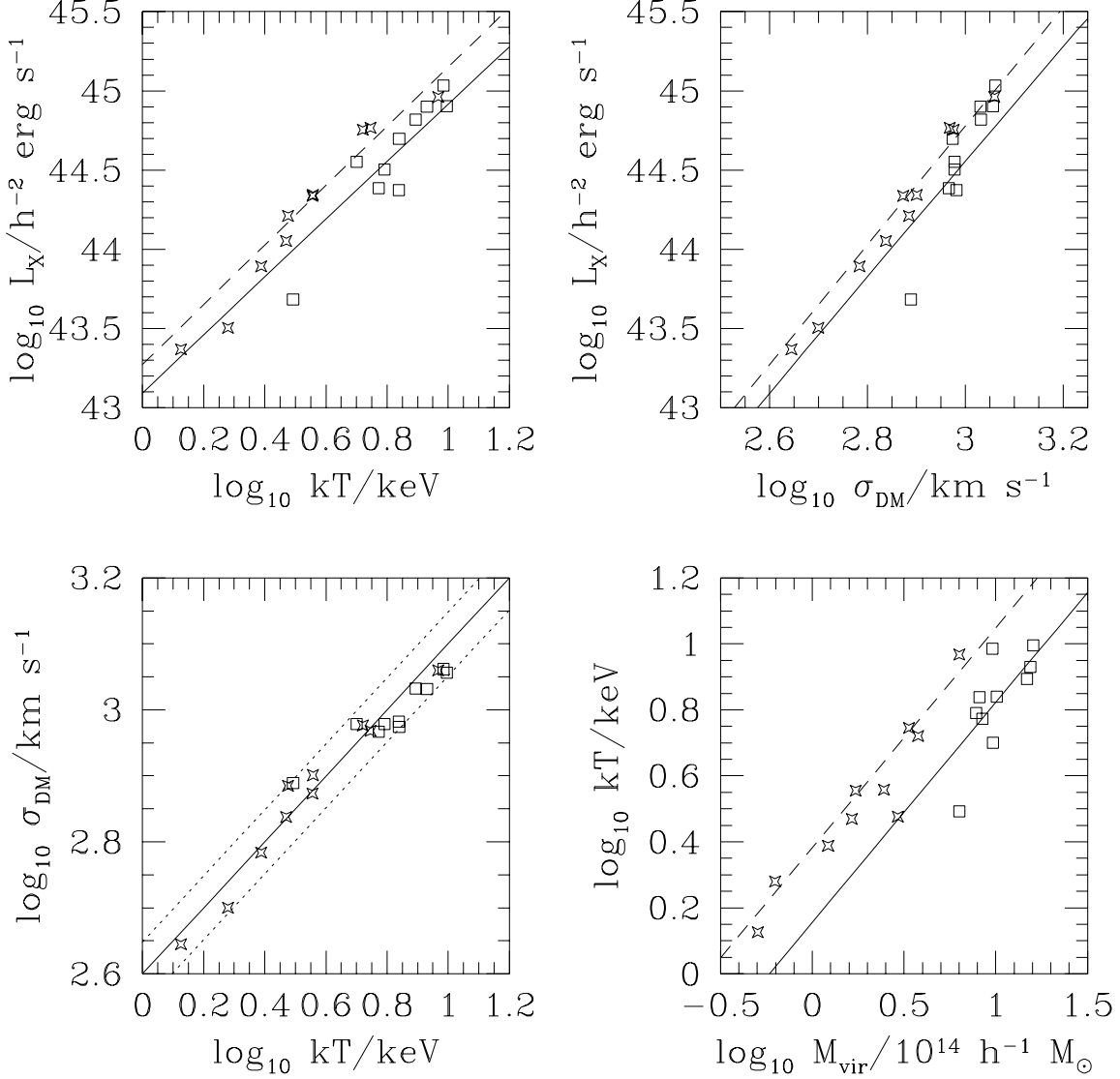


Fig. 13.— Correlations between cluster properties at  $z=0$  (open squares) and at  $z=1.09$  (starred symbols).  $M_{\text{vir}}$  is the virial mass,  $kT$  is the X-ray emission-weighted temperature,  $\sigma_{\text{DM}}$  is the one-dimensional velocity dispersion of the dark matter, and  $L_X$  is the X-ray bolometric luminosity of each cluster. The solid lines show the scaling laws described in §2 at  $z=0$  and the dashed lines at  $z=1.09$ . The zero point of the scaling laws involving  $L_X$  is arbitrary and has been chosen to provide the best fit to the  $z=0$  clusters. The  $z=1.09$  curves are derived using the redshift dependence described in §2. Note that in general the results of the numerical simulations follow closely the expected evolution.

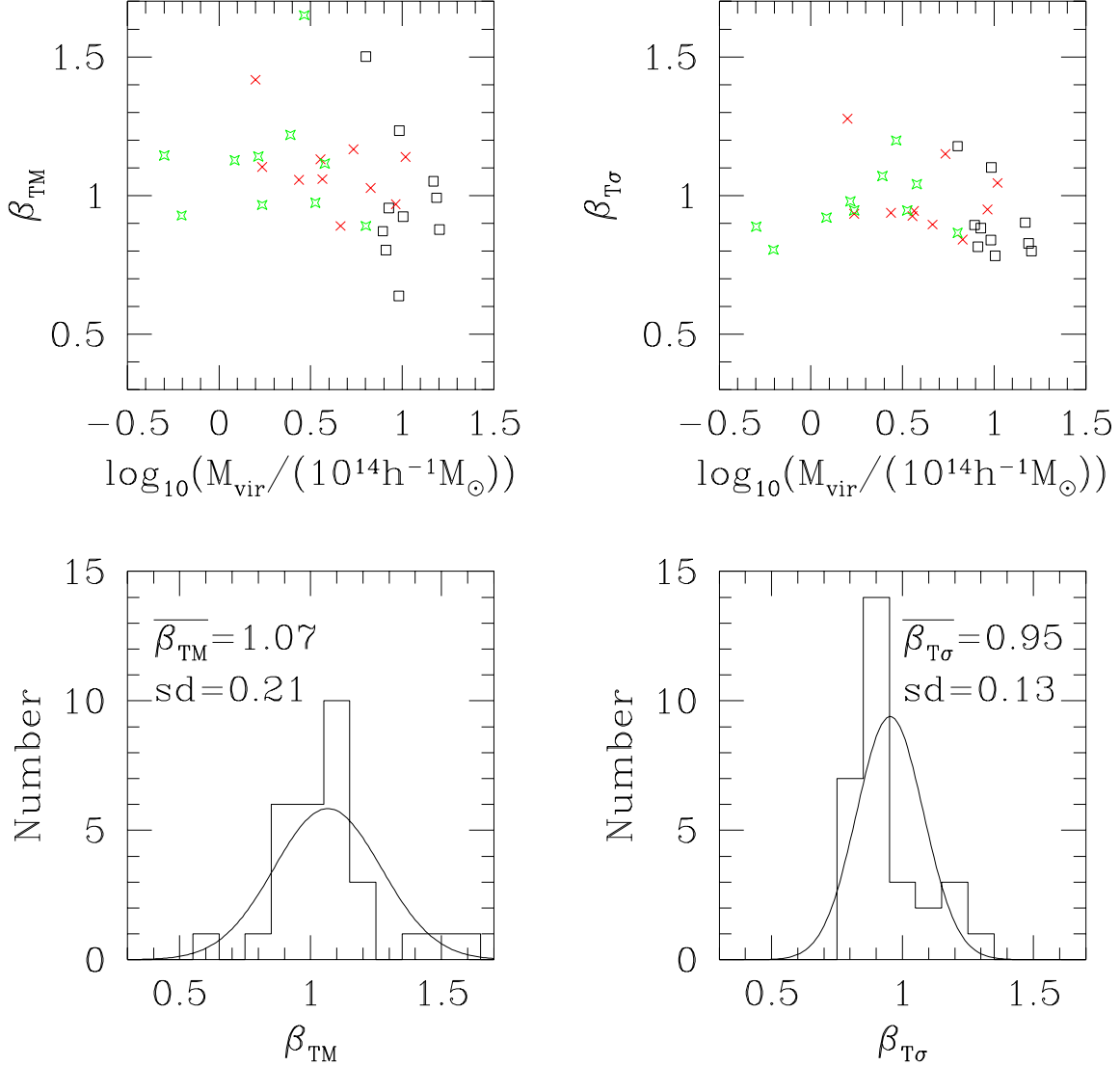


Fig. 14.— Mass and redshift dependence of the parameters  $\beta_{T\sigma}$  and  $\beta_{TM}$ , defined by eqs.(18) and (19), respectively. These parameters relate the X-ray emission-weighted temperature to the velocity dispersion of the dark matter and to the virial mass of the cluster. Open squares, crosses, and starred symbols are used to represent clusters at  $z = 0$ ,  $0.38$ , and  $z = 1.09$ , respectively. A histogram is shown in the second row, together with the best-fitting Gaussian distribution. The average value of  $\beta_{T\sigma}$  is independent of redshift, and is consistent with unity. The average value of  $\beta_{TM}$  is also consistent with unity, but with somewhat larger scatter. The latter appears to decrease with redshift, by only slightly more than 10% from  $z \sim 1$  to the present.



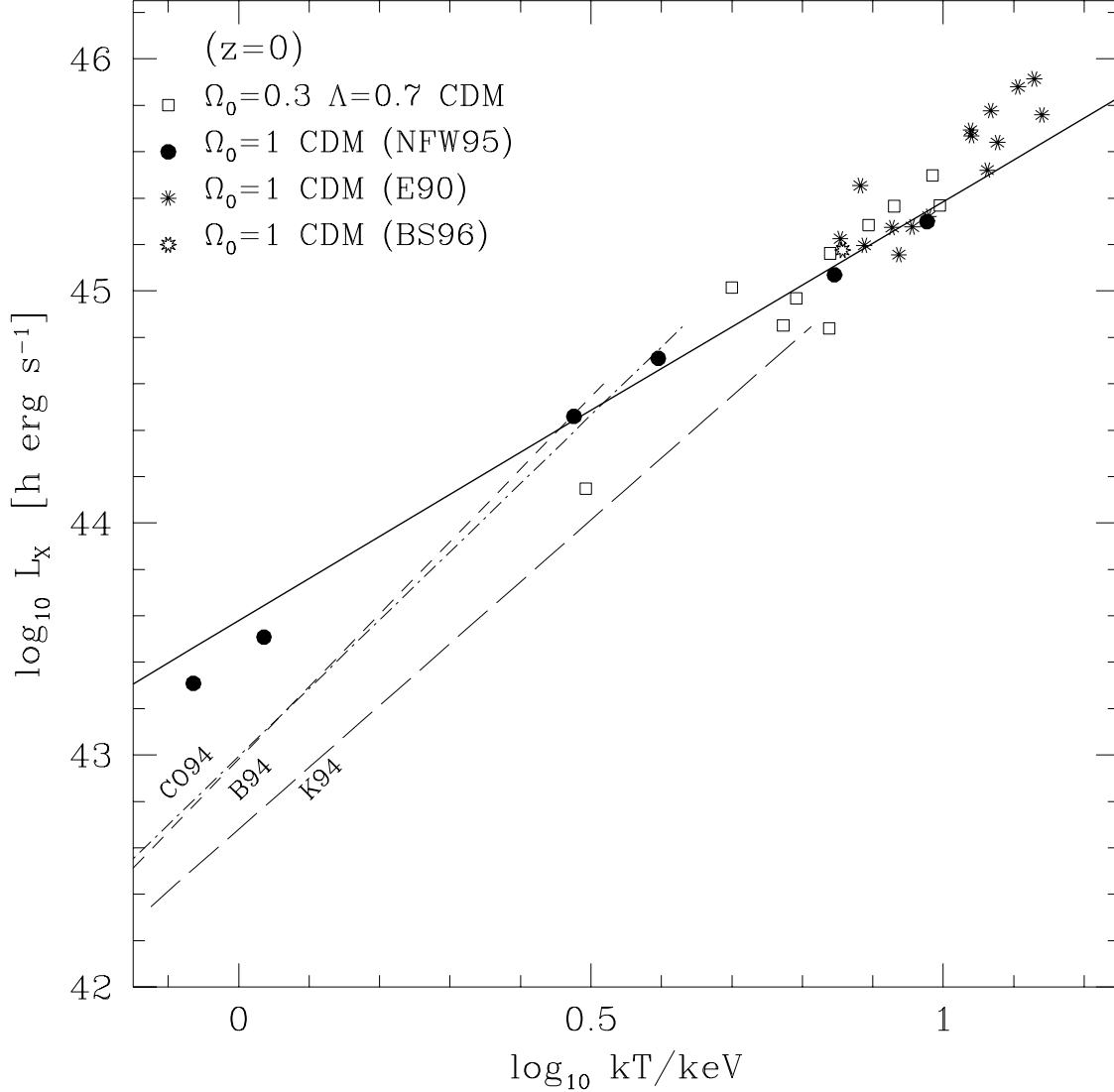


Fig. 15.— The luminosity-temperature relation at  $z = 0$  compared with results from other published simulations. The open squares refer to this work and are fitted by the solid line, as explained in the caption to Figure 13. The solid circles show results from Navarro *et al.* (1995, NFW95). Other symbols correspond to Evrard (1990, E90) and Bartelmann & Steinmetz (1996, BS96). The curve labeled CO94 corresponds to the  $\Omega_0 = 0.45$ ,  $\Lambda = 0.55$  CDM simulations of Cen & Ostriker (1994). The curves labeled K94 and B94 correspond to the  $\Omega_0 = 1$  CDM simulations of Kang *et al* (1994), and Bryan *et al* (1994), respectively. Results from CO94, K94, and B94 are shown over the range in luminosities actually probed by their simulations. All luminosities have been scaled to the same gas fraction ( $f_{\text{gas}} = 0.1$ ) for comparison. Luminosities are given in units of  $h \text{ erg s}^{-1}$  so that, at fixed T, clusters of similar density contrasts will have comparable luminosities.

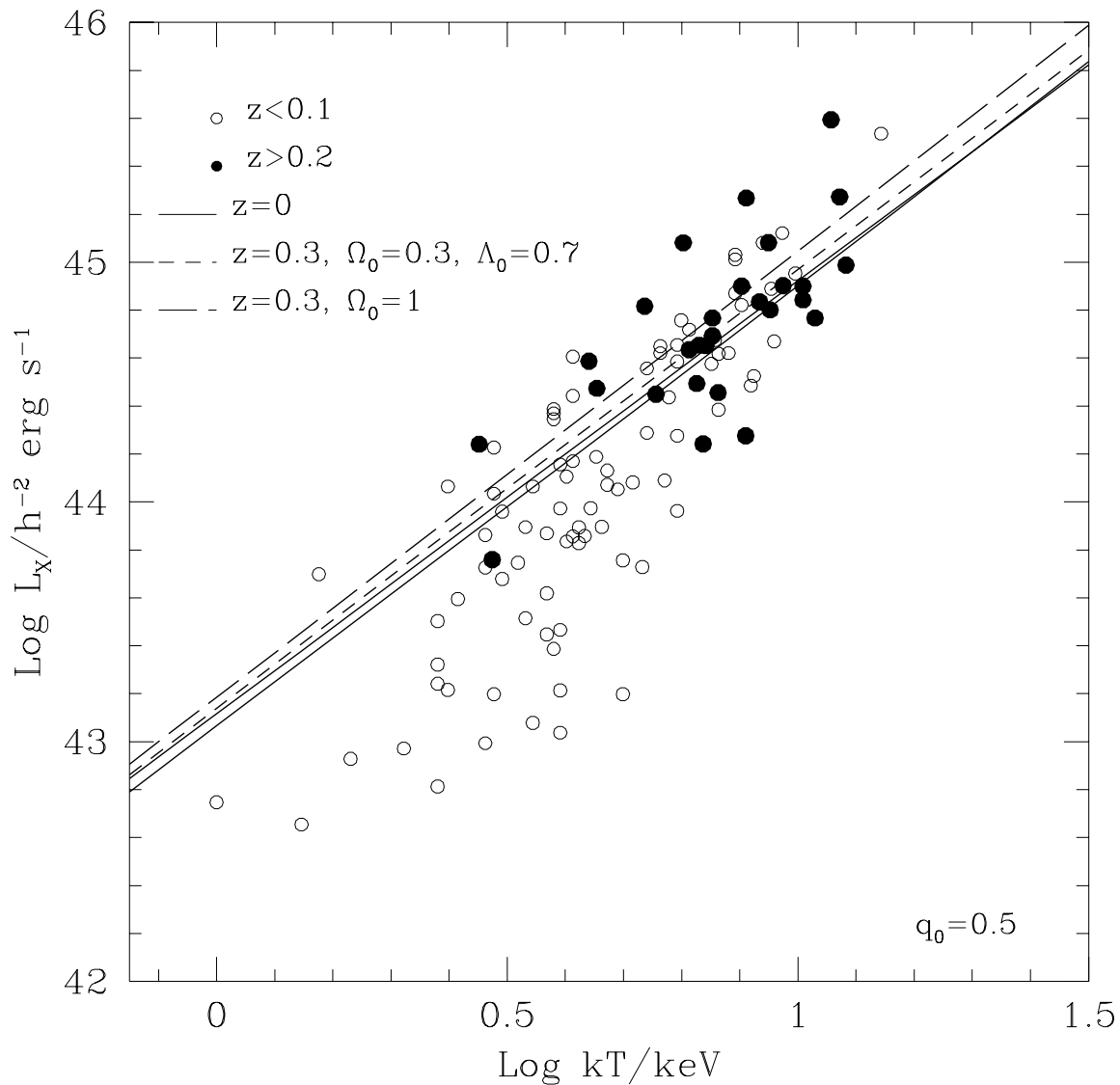


Fig. 16.— Evolution of the luminosity-temperature relation predicted by the scaling laws derived in §2, compared with observations. Bolometric luminosities and temperatures were taken from the compilations by David *et al.* (1993) and Mushotzky & Scharf (1997). High-redshift ( $z > 0.2$ ) clusters are shown with solid circles and low-redshift ( $z < 0.1$ ) clusters with open circles. All observed luminosities have been scaled to a common value of  $q_0 = 0.5$  for comparison. Predictions for  $z = 0$  (solid lines) and  $z = 0.3$  (dashed lines) are shown for two CDM cosmologies:  $\Omega_0 = 1$  and  $\Omega_0 = 0.3, \Lambda = 0.7$ . At  $z = 0$  the predictions of both models have been normalized to match our simulations, as described in Figure 13. The predicted slope is too shallow to be consistent with observations: clusters with  $kT < 5$  keV are systematically fainter than expected. In both cosmologies clusters are expected to be slightly more luminous in the past, although the effect at  $z \sim 0.3$  is small and would be difficult to detect observationally.

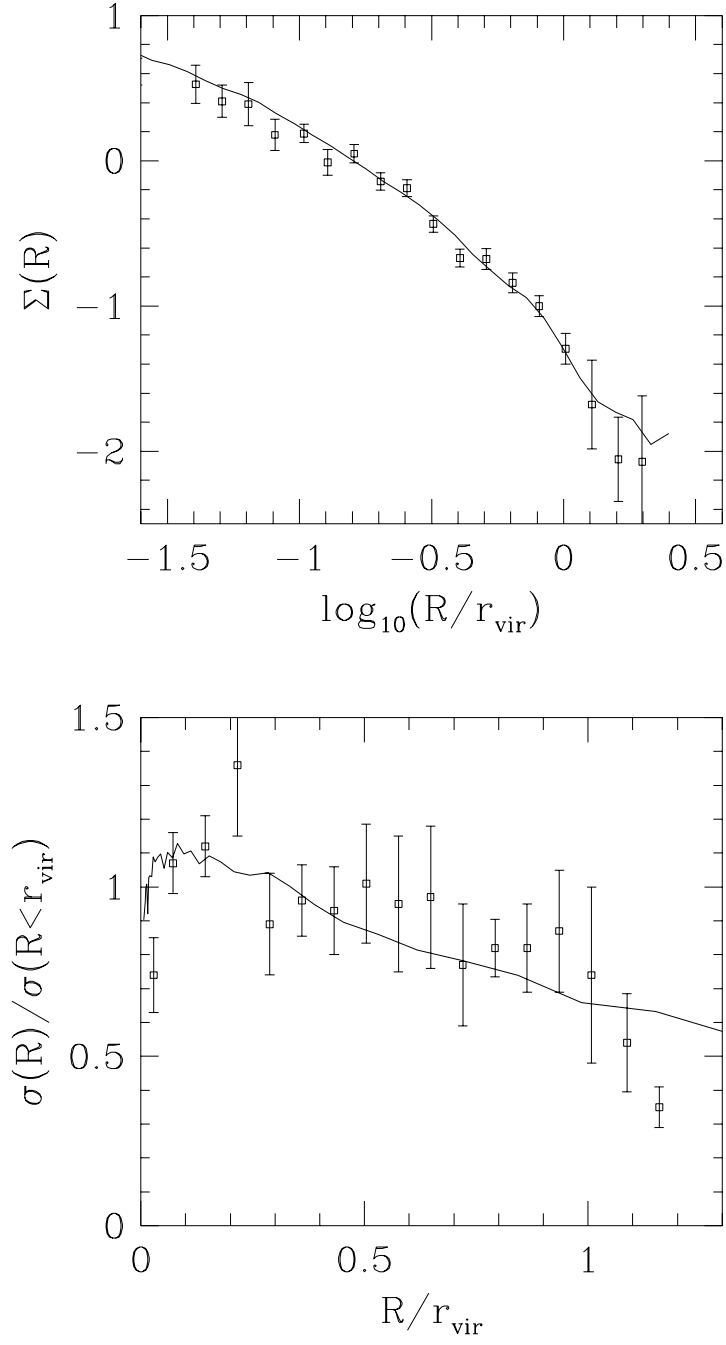


Fig. 17.— Top panel: projected dark matter density profiles, averaged over different projections of the ten simulated clusters (solid lines) displayed on top of the galaxy number density profile of CNOC clusters (Carlberg *et al.* 1997). The vertical scale is arbitrary, and has been chosen to match simulations and observations. Bottom panel: as above, but for the line-of-sight velocity dispersion profiles. There are no free rescalings in this lower panel. The excellent agreement between galaxy and dark matter profiles suggests that galaxies are essentially unbiased tracers of the mass in these clusters.